3 The terbium bis(phthalocyaninato) complex

3.1 Introduction

The Terbium bis(phthalocyaninato) complex ($TbPc_2$) is a one of the most investigated SMM [1]. Thanks to its magnetic properties the $TbPc_2$ molecule, and its derivatives, is a promising candidates for spintronic purposes [2–4]. The $TbPc_2$ molecule belongs to the metal double decker class in which a Tb^{3+} ion is bound in the centre of two phthalocyanine molecules staggered 45° by each other, as show in fig. 3.1.

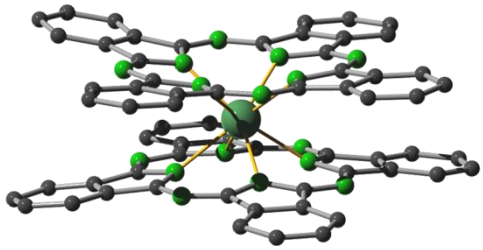

Fig. 3.1: Terbium bis(phtahalocyaninato) complex ($TbPc_2$) structure.

$TbPc_2$ can be easily synthesised as neutral $[TbPc_2]^0$ and cationic $[TbPc_2]^{-1}$ powder, as described in the next chapter [5,6]. By chemical oxidation of $[TbPc_2]^0$ [7] or by electrochemical synthesis [8,9] is also possible to achieve the $[TbPc_2]^{+1}$ compound which is not stable, behaving as strong oxidative molecule. It is important to note that the oxidation number of the metal ion does not change passing from the oxidised $[TbPc_2]^{+1}$ to the reduced $[TbPc_2]^{-1}$ molecule because the oxidation/reduction process involves only the electronic structure of the ligands [9].

The magnetism of the $TbPc_2$ molecules derives from the large magnetic moment and the huge magnetic anisotropy of the lanthanide ion. The molecule is characterised by strong uniaxial anisotropy with the easy axis of magnetisation along the idealised C_4 rotation axis. The ground state manifold for the $4f^8$ electronic configuration is characterised by J = L+ S = 6, which is split by the crystal field at the single Tb^{3+} ion. This results in a separation between the ground doublet, well described by Jz = ±6, and the first excited state on the order of a few hundred Kelvin [1,7]. In the $[TbPc_2]^0$ a second spin system is defined by the presence of an unpaired electron delocalized on the π system of the phthalocyanine ligands [6,10]. Some differences in the magnetic behaviour of the three oxidation forms of the $TbPc_2$ are reported in literature. In particular the oxidation process leads to an increase of the barrier opposing the reversal of the magnetisation [7]. By DFT theoretical calculations Ishikawa and co. [11] have showed that the oxidation process leads to a shrink of the interplanar distance between the two phthalocyanine ligands, suggesting an increase of the crystal field applied to the Tb^{3+}. The hysteresis loops of the $[TbPc_2]^{-1}$ and $[TbPc_2]^{+1}$, investigated by magnetic circular dichroism (MCD) of frozen solutions, show the presence of the so called butterfly hysteresis shape [8], which is characterised by the presence of moderate tunnelling in zero field. Similar behaviour is detected also in $[TbPc_2]^0$ as reported in section 3.2.

The high chemical stability of the MPc_2 class allows the $[TbPc_2]^0$ to be thermal sublimated in ultra-high vacuum (UHV) as well as in high vacuum (HV) conditions [6,12–14]. This property boosted the studies of the $[TbPc_2]^0$ allowing the preparation of many different hybrid surface made by molecules deposited on solid substrates. Thanks to the flat shape of the molecules, that facilitates the imaging, detailed scanning tunnelling microscopy (STM) investigations have been carried out. In thin film of MPc_2 sublimated on different metal surfaces [12,14–17] the molecules lay flat with one of the two phthalocyanine ligand facing the surface. In the case of $TbPc_2$ the easy axis is pointing out of the surface plane. By STM

imaging the single $TbPc_2$ molecule looks as four-lobed structure when imaged in low bias or in low resolution images whereas in high resolution images eight-lobed structure is commonly observed [16].

In scanning tunnelling spectroscopy (STS) experiments the orbital energies can be easily detected [5,15,16] while in zero bias region a Kondo peak, due to the presence of the unpaired electron on the ligands, is revealed in $TbPc_2$ molecule sublimated on Au(111) [5,18]. However the presence of the unpaired electron may be altered on absorption on surface so that in $TbPc_2$ molecules sublimated on Co grown on Ir(111) it is quenched [17].

In parallel the magnetic characterisation of such hybrid surfaces has been carried out. For this purpose one of the mostly employed techniques is the X-ray circular dichroism (XMCD), thanks to the element selectivity and the high sensitivity, which allows the characterisation of sub-monolayer films [19,20]. On metal surfaces the XMCD derived hysteresis loops acquired in sub-monolayer/monolayer samples showed no opening [13,14,21,22], while on thicker film the hysteresis opening is recovered [13]. This anomalous behaviour has been investigated but by thus far no clear explanation is reported. In order to rationalize it a key role of molecule-surface and molecule-molecule interactions has been proposed. The presence of molecule-surface interactions has been recently reported to play a key role in the prominent antiferromagnetic (AF) coupling observed in sub-monolayer film of $TbPc_2$ sublimated on nickel [21], and in the observation of an exchange bias on thin film sublimated on manganese [22]. Moreover the molecule-molecule interactions are responsible of the different magnetic behaviour of the isostructural paramagnetic YPc_2 molecule in solvated and non-solvated crystallographic phase [23].

The preferential orientation of the $TbPc_2$ molecules in thin and thick films has been investigated by X-ray linear natural dichroism. In agreement with the STM characterisation in thin film the molecules are lying flat, on the contrary in the thick film a preferential orientation in “standing-up” geometry has been revealed [13]. This is not surprising; it is well known that for simple phthalocyanine

during the films grown a molecular reorientation process occurs [24]. In fact for the copper phthalocyanine (CoPc) complexes, synchrotron based investigations using near-edge X-ray absorption fine structure spectroscopy and surface sensitive X-ray photoemission spectroscopy experiments revealed that these flat molecules start to lose their lying orientation on Au(111) substrates after 3ML and that the standing orientation is fully retrieved after ca. 10 ML [25]. This structural change obviously alters the molecule-molecule interactions and a non-negligible effect on the behaviour of the $TbPc_2$ can be anticipated.

In order to shed some light on this phenomenon we have studied the magnetic properties of the $TbPc_2$ molecule starting from the characterisation of the pristine microcrystalline powder, throughout the sublimation process to the final film samples. We have also investigated the magnetic behaviour of thin films sublimated on two of the most employed magnetic substrate in spintronic devices. This characterisation was performed in order to prepare the ground for the employment of the $TbPc_2$ as organic layer in spin valve device (see section 3.4).

3.2 Erratic magnetic hysteresis

3.2.1 $TbPc_2$ synthesis

The neutral $MPc_2{\cdot}CH_2Cl_2$(M = Tb^{3+} and Y^{3+}) compounds were synthesised according to the procedure reported in literature [5,6]. The template reaction was carried out by mixing 1,2-dicyanobenzene and $M(OAc)_3 \cdot 4H_2O$ in 1-hexanol in presence of catalytic amount of 1,8-diazabicyclo[5,4,0]undec-7-ene (DBU) as represented in fig. 3.2.

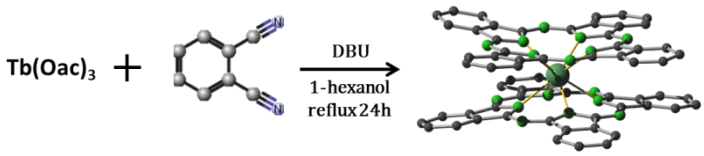

Fig. 3.2: Terbium bis(phtahalocyaninato) complex ($TbPc_2$) synthesis reaction scheme.

It was used 8:1 1,2-dicyanobenzene : $M(OAc)_3 \cdot 4H_2O$ molar ratio in order to limit the formation of M_2Pc_3 molecules. The mixture was refluxed for at least 1 day. Once at room temperature it was filtered and the precipitate was washed with acetic anhydride, cold acetone, and n-pentane in sequence. The precipitate was extracted with several portion of $CHCl_3$. The neutral $[TbPc_2]^0$ and the anionic one $[TbPc_2]^{-1}$ reside in the solution while most of the free phthalocyanines reside in the solid phase. The solution was then concentrated and purified by chromatography. The column was prepared using silica as stationary phase and 98:2 CH_2Cl_2/MeOH solution was employed as eluent. The first green fraction collected contains the $[TbPc_2]^0$ whereas the second blue fraction is the $[TbPc_2]^{-1}$. The green solution was then concentrated. By addition of n-Hexane a dark microcrystalline powder of $[TbPc_2]^0 \cdot CH_2Cl_2$ was precipitated. After filtration the powder was left to dry in air before being used.

The powder of the neutral complex was solubilized in $CHCl_3$ in order to recorder the UV/visible absorption spectrum (fig. 3.3) to confirm the quality of the neutral compound [8].

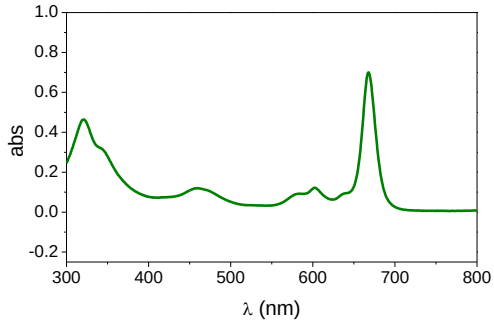

Fig 3.3: UV/vis spectrum of a solution of $[TbPc_2]^0$ in $CHCl_3$.

To have more insight on the UV/vis spectrum peaks attribution see section 3.2.6.

3.2.2 Microcrystalline $[TbPc_2]^0 \cdot CH_2Cl_2$ hysteresis

The magnetic properties of a microcrystalline powder sample of $[TbPc_2]^0 \cdot CH_2Cl_2$, hereafter simply $TbPc_2 \cdot CH_2Cl_2$, were investigating by using a vibrating sample magnetometer (VSM see chapter 2.1.1). On the left of fig. 3.4 left it is reported the temperature dependence of the hysteretic loops recorded using a field-sweeping rate of 50 Oe s^{-1}. At 25 K the curve shows a paramagnetic behaviour with linear field dependence of the magnetisation. Just decreasing the temperature to 15 K a small hysteretic behaviour is detected and between 10 K and 2 K the so called butterfly shape hysteresis is well visible. It is interesting to note that the temperature dependence of the area inside the hysteretic loops is not monotone (fig. 3.4 right). Starting from 2 K the area increases until reaching the maximum value at 5 K and then it shrinks asymptotically increasing the temperature. The hysteresis loops presented in fig. 3.4 left are taken as reference for further comparison.

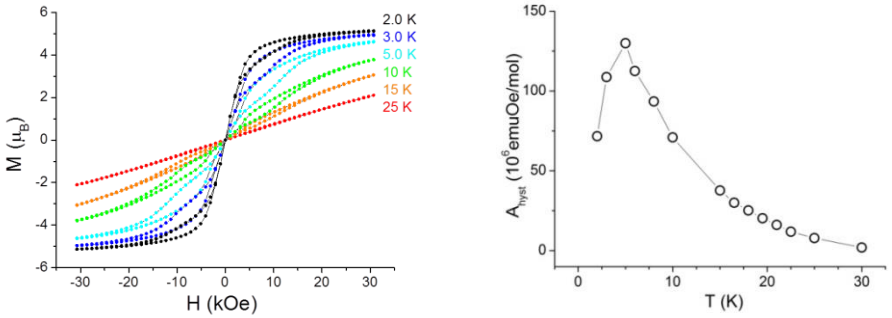

Fig 3.4: Temperature dependence of the hysteresis loops recorded on $[TbPc_2]^0 \cdot CH_2Cl_2$ a pure microcrystalline powder sample (left) the data are reported per mole of $TbPc_2$ and the field sweeping rate is 50 Oe s^{-1}; Temperature dependence of the area inside the hysteresis loops (right). The line is only a guide to the eye.

3.2.3 Sublimation process: $TbPc_2$ hysteresis transformation

As stated in section 3.1 $TbPc_2$ SMMs have attracted a growing interest thanks to their thermal stability which allow the sublimation of intact molecules in HV condition [6,12–14]. We studied how the thermal treatment affects the hysteresis behaviour of this SMM. Using the sublimation system reported in section 2.2 the pristine powder of $TbPc_2{\cdot}CH_2Cl_2$ was degased at 580K for several hours in HV condition (pressure < $5x10^{-7}$mbar). It was then warmed up to the sublimation temperature of about 670 K for few minutes and finally allowed to cool to room temperature. The XRD analysis of the heated powder is reported in fig. 3.5 together with the spectrum of the pristine powder.

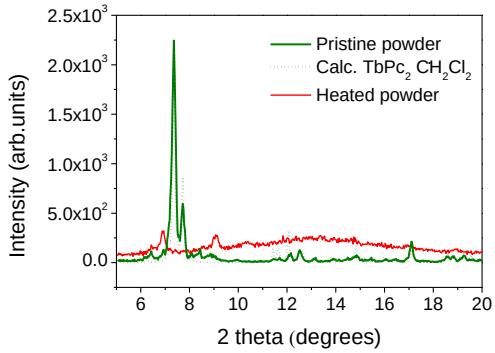

Fig 3.5: XRD spectra of: pristine (green), $TbPc_2{\cdot}CH_2Cl_2$ calculated (dot black), and heated sample (red). The pristine powder spectrum matches the calculated one while the heated powder spectrum is amorphous like.

As expected the pristine powder spectrum matches the simulated one for a crystalline powder, while, on the other hand, the heated sample looks like an amorphous phase. The lack of crystalline structure could be related to the loss of the crystallization solvent (CH_2Cl_2) during the heating procedure.

The heated powder was characterised by VSM technique (fig. 3.6 left) repeating the measurements carried out on the pristine sample. The temperature dependent hysteresis loops unexpectedly show no hysteresis opening throughout the whole temperature range.

In order to check the intactness of the molecules in the sample a thick film of $TbPc_2$ was sublimated on Kapton using the heated powder. The temperature dependence of the hysteretic loops is reported in fig. 3.6 right. The curves show the recovery of the hysteretic behaviour. The opening is detected at temperatures as high as 10 K, slightly lower than in the pristine microcrystalline powder, and a monotone dependence of the insight area on temperature throughout the investigated range is observed. Despite these differences the presence of the hysteresis opening suggests that the heated powder comprises intact molecules.

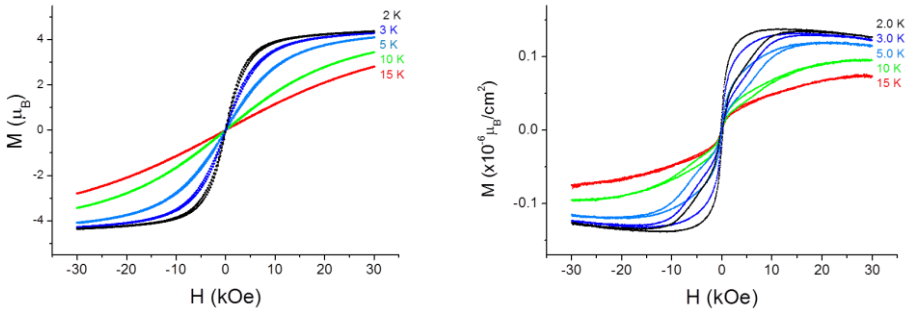

Fig 3.6: Temperature dependence of the hysteresis loops recorded on the heated powder of $TbPc_2$ (left) taken out from the crucible before the sublimation of the molecules and on a film of $TbPc_2$ evaporated on Kapton (left). The data are reported per mole of $TbPc_2$ in (left) and per square centimetre of the film in (right). The field sweeping rate is 50 Oe s^{-1}.

The different behaviours shown by the three samples of $TbPc_2$ must be related to different dynamic relaxation processes operating in the three different phases. In order to explain these anomalies and further confirm the presence of intact molecules in the heated powder the ac susceptibility was investigated. The measurements were carried out from 0.5 Hz up to 10 kHz in 5–100 K temperature range on both powder samples, pristine and heated, respectively. No further measurements were carried out on the $TbPc_2$ film because it showed too small magnetic signal for a complete *ac* susceptibility investigation. Both powders show an out of phase component of the susceptibility in zero field which is the fingerprint of the SMM behaviour (fig. 3.7).

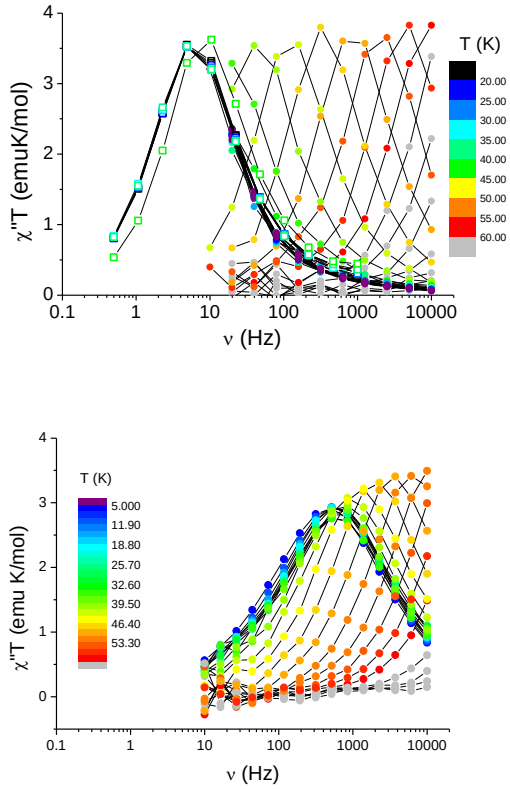

Fig 3.7: Frequency dependence of the product of temperature with the out-of-phase component of the magnetic susceptibility of $TbPc_2 \cdot CH_2Cl_2$ (Top) and of the heated powder (down); measured in zero static field.

Decreasing the temperature the maximum shifts to lower frequency and below 40 K no dependence is detected in agreement to the onset of the tunnelling regime between the two quasi-degenerate $m_J = \pm 6$ ground states [26].

The χ''curves were fitted by using the extended Debye model [27,28]:

$$\chi'' = (\chi_T - \chi_S)\frac{(\omega\tau)^{1-\alpha}\cos(\pi\alpha/2)}{1+2(\omega\tau)^{1-\alpha}\sin\left(\pi\frac{\alpha}{2}\right)+(\omega\tau)^{2-2\alpha}} \qquad (3.1)$$

where ω is the angular frequency, τ is the relaxation time, χ_T and χ_S are the isothermal and adiabatic limits respectively while the α

parameter is related to the width of the τ distribution. The temperature dependence the τ distribution is depicted in fig. 3.8.

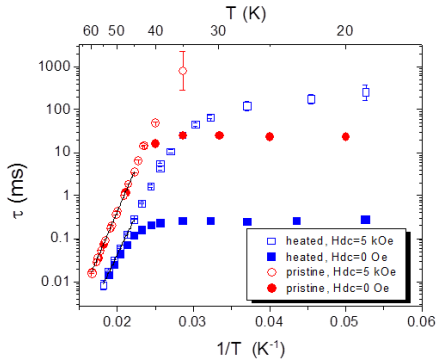

Fig 3.8: Temperature dependence of the relaxation time extracted from ac susceptibility data on the pristine (red) and heated (blue) $TbPc_2$ samples. The empty symbols correspond to the measurement in a static magnetic field of 5 kOe. The black lines correspond to the best fit curves using the Arrhenius law on the high temperature data under a static magnetic field.

Below 40 K the relaxation mechanism of both powders in zero field is dominated by tunnelling but the process in the heated powder is 10^2 faster (table 3.1).

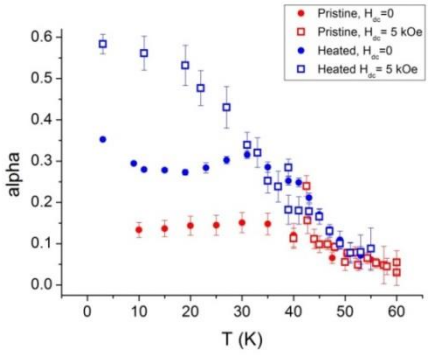

Fig 3.9: Temperature dependence of the parameter describing the width of the distribution of relaxation time extracted from the simulation of the out-of-phase component of the ac susceptibility according to the extended Debye model.

In fig. 3.9 are reported the α values vs T. It is interesting to note that in the tunnelling regime the α value is almost doubled, ca. 0.3 vs 0.15, in the heated sample, in agreement with its amorphous state.

By applying a static field of 5 kOe, which corresponds to the maximum hysteresis opening of the pristine sample, the tunnelling process is partially suppresses and a more precise analysis of the

temperature dependence of the relaxation time can be performed. Above 40 K τ is found to follow the Arrhenius law, in agreement with previous experiments. However, while it levels off below 30 K in the heated powder, with a gradual increase of α, it continues to diverge, at least within the time window accessible in our experiment, for the pristine powder. This different behaviour justifies the disappearance of the hysteresis of the heated sample as due to a more pronounced tunnelling in field of the thermally treated sample. From table 3.1 we can notice that the activation barrier is slightly smaller for the heated sample. It should be however considered that the effects of the more pronounced tunnelling can influence the estimation of the barrier.

	τ_0(s)[a]	Δ(K)[a]	Γ_{qt}(s^{-1})[b]
Pristine	$1.85(5)\times10^{-12}$	965(20)	42
Heated	$1.5(1)\times10^{-12}$	856(20)	3660

[a] Extracted from data taken at H_{dc}=5 kOe

[b] Measured in zero static field.

Table 3.1: Parameters of the magnetisation dynamics extracted from ac susceptibility data for pristine and heated samples of $TbPc_2 \cdot CH_2Cl_2$.

These data highlight different relaxation dynamics operating in the two bulk samples, which differ in their structure i.e. microcrystalline and amorphous. The evaporated film shows a behaviour more similar to that of the pristine material. This observation suggests a more regular packing of the molecules in the film, a feature that is common to metal-phthalocyaninato (MPc)-based films, although the same crystal structure of the pristine compound cannot be achieved due to the loss of CH_2Cl_2 during the heating process.

In order to have some insight two different studies were carried out. A thick film of $TbPc_2$ evaporated on quartz was characterised by magnetic circular dichroism (MCD) (see section 3.2.6). Just for clarity of the discussion we anticipate that on all evaporated samples at least a preferential orientation of the molecules respect to the substrate surface is detected. This supports the presence of a certain degree of order inside the film that correlates to the magnetic properties. This

is not surprising, in fact Katoh et al. extensively investigated double and multi-decker lanthanide complexes and evidenced a significant dependence of the magnetisation dynamics on the crystal packing, suggesting a key role of Ln–Ln dipolar interactions [29]. A similar trend has also been observed for other single ion slow relaxing species [30,31], like Er^{3+} polyoxometalate [32] and the Dy^{3+} complex with the DOTA ligand [33].

3.2.4 $TbPc_2$ in magnetic dilution environment

In order to have some insight on the role played by intermolecular interactions a dilution study was performed. It is well know that the magnetisation dynamics is sensitive to dilution in diamagnetic hosts [34]. The tunnelling efficiency strictly depends to the relative energies of the levels on the opposite side of the anisotropy barrier. The local dipolar fields generated by other $TbPc_2$ molecules can modify the gap energy of the levels involved in the tunnelling process. This dipolar interaction mechanism is particularly efficient in case of the fields aligned to the easy axis of the molecule, which can tune the gap energy by bringing the levels in or out of resonance; thus modifying the magnetisation dynamics [27]. On the other hand exchange interactions, which can be mediated by the unpaired electron residing on the phathalocyanine rings, must be taken in account. The dilution in diamagnetic hosts leads to an insulation of the $TbPc_2$ molecules hindering the dipolar interaction as well the exchange ones.

Two types of dilution were performed by dispersing the pristine powder of $TbPc_2{\cdot}CH_2Cl_2$ in a Poly(methyl methacrylate) (PMMA) polymeric matrix and by preparing Tb-doped YPc_2 sample. The PMMA matrix was preferred respect to a frozen solution for practical purposes. In fact, during the formation of the dispersed sample, either by polymerization or by cooling down the diluted solution, the formation of micro-crystallites can occur. The polymeric matrix allows inspection by optical microscope and X-ray micro-

analysis in order to check their formation, while for the frozen solution the same characterisation is more complicated.

By employing these techniques the threshold concentration for the micro-crystallites formation was estimated above 0.2 wt %, within the resolution limit of 700 nm of the X-ray micro-analysis. The hysteresis loops recorded for two samples, namely 1 wt % and 0.2 wt %, are depicted in fig 3.10. The concentrated sample presents the micro-crystallites formation while no crystallites were revealed for the diluted one. The reported data are not corrected by the diamagnetic contribution of the polymeric matrix, which is more pronounced in the diluted sample. Nevertheless significant differences are evidenced. The concentrated sample shows a hysteresis opening already at 15 K and the presence of significant butterfly hysteresis for lower temperature. It is also interesting to note the no linearly dependence of the area inside the hysteresis on the temperature for the concentrated sample. This behaviour is similar to that observed for the pristine microcrystalline powder. On the contrary the proper diluted sample (0.2 wt %) shows no hysteresis opening above 5 K and a less pronounced tunnelling relaxation in zero field. This findings is in agreement to that observed by MCD experiments on a frozen solution of $TbPc_2$ in CH_2Cl_2 [8], and suggests that an efficient magnetic insulation of these SMMs induces a reduction of the tunnelling probability.

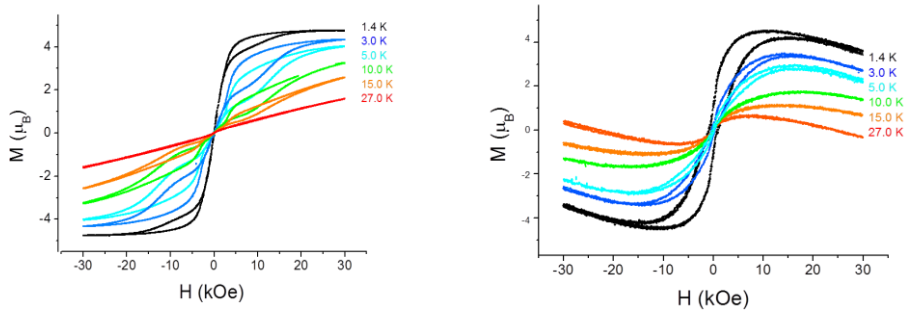

Fig 3.10: Temperature dependence of the hysteresis loops recorded on $TbPc_2 \cdot CH_2Cl_2$ dispersed in PMMA at 1% in weight concentration (left) and 0.1% (right). In the 1 % sample aggregates are formed. The data are reported per mole of $TbPc_2$ and the field sweeping rate is 50 Oe s^{-1}.

In the second experiment a solid solution of $TbPc_2$ in $YPc_2{\cdot}CH_2Cl_2$ was prepared. In order to achieve 10:90 $TbPc_2$:YPc_2 ratio the synthesis reported in section 3.2.1 was employed. $YPc_2{\cdot}CH_2Cl_2$ crystals are isomorphous to the $TbPc_2$ analogue and they show a paramagnetic behaviour due to the unpaired electron on the phathalocyanine rings. In the right part of the fig. 3.11 the temperature dependence of the hysteresis loops of the $Tb_xY_{1-x}Pc_2{\cdot}CH_2Cl_2$ is reported to be compared to the reference data of the pristine $TbPc_2{\cdot}CH_2Cl_2$ sample (fig. 3.4 left). The diluted data are not corrected for the paramagnetic behaviour of the YPc_2 molecules and they are plotted for mole of $TbPc_2$; therefore the magnetisation value results higher because the paramagnetic contribution of ca. 9 moles of the YPc_2 radicals is added for each $TbPc_2$ mole. However, as far as hysteretic behaviour is concerned, no significant differences are observed.

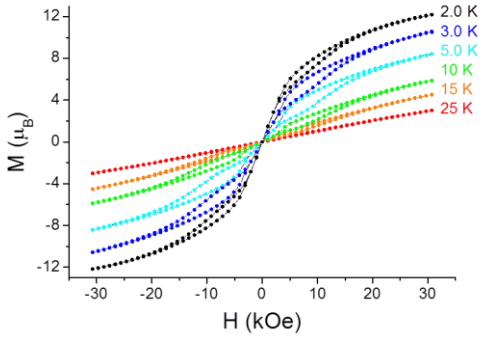

Fig 3.11: Temperature dependence of the hysteresis loops recorded on $Tb_xY_{1-x}Pc_2{\cdot}CH_2Cl_2$. The data are reported per mole of $TbPc_2$ and the field sweeping rate is 50 Oe s^{-1}.

This remarkable finding suggests that dipolar interactions, due to neighbouring Tb^{3+} ions, do not significantly influence the magnetisation dynamics of $TbPc_2$ in the investigated temperature range. This is in contrast to some differences observed by Ishikawa et al. [35] in the mK temperature region and to what reported for the octabutoxy-phthalocyaninato derivative [29]. Although the dipolar interactions, significantly reduced in the doped system, are not significantly affecting the relaxation dynamics, nothing can be said about the intermolecular exchange interactions. These are in fact

mediated by the π stacking of Pc ligands and are therefore expected to be partially active also in the $Tb_xY_{1-x}Pc_2{\cdot}CH_2Cl_2$ sample.

3.2.5 Evaluation of the exchange interaction

In order to investigate the role of the exchange interactions in the dynamic relaxation process of $TbPc_2$ SMMs in different packing environments the YPc_2 derivative was chosen as reference. It is already mentioned that this is a paramagnet molecule isostructural to $TbPc_2$. It sounds reasonable to assume that the exchange intermolecular interactions in the YPc_2 and $TbPc_2$ are comparable, with the latter experiencing also significant dipolar interactions due to the large moment of Tb^{3+}.

It is known that the $YPc_2{\cdot}CH_2Cl_2$ crystals at intermediate temperatures show a weak ferromagnetic interaction between molecules aligned along the crystal columns, while below 1.35K the onset of three-dimensional antiferromagnetic (AF) order was observed [23]. On the contrary YPc_2 crystallizing in the $P2_12_12_1$ space group, which correspond to the crystalline phase without the CH_2CH_2 solvent, exhibits AF interaction in the whole range of temperature as reported by Paillaud et al. [23] and recently confirmed by solid state NMR characterisation [36].

We decided therefore to investigate how the sublimation process influences the exchange interactions between YPc_2 radicals. The χT products of the pristine $YPc_2{\cdot}CH_2Cl_2$ microcrystalline powder, which shows the expected ferromagnetic behaviour in the investigated temperature range, is reported in fig. 3.12 (blue). The χT product for the heated powder and for a film prepared by sublimation of YPc_2 on Teflon tape are also reported in fig. 3.12. The χT product of heated powder decreases by decreasing the temperature. Thus, it shows the expected antiferromagnetic behaviour for YPc_2 powder without CH_2Cl_2 molecules of crystallization [23]. Since the YPc_2 susceptibility is ca. 40 times smaller than that of $TbPc_2$ the detection of sublimated films is quite challenging. In order to achieve a suitable

µm film thickness a long sublimation process was carried out on µm film of Teflon tape. This minimises the diamagnetic contribution of the substrate. Although less pronounced than in the heated powder case, the χT product dependence on the temperature of the film shows intermolecular antiferromagnetic interactions. The data were fitted by using the Curie–Wiess law:

$$\chi = \frac{C}{T-\theta} \qquad (3.2)$$

The Weiss constants θ extrapolated are 0.22(1) K, −4.1(1) K, and −2.5(1) K for the pristine powder, heated powder, and evaporated film, respectively.

Assuming that the intermolecular exchange interactions between the paramagnetic ligands are comparable in isostructural $TbPc_2$, our observation suggests that no clear correlations exist between the strength and nature of these interactions and the disappearance of hysteresis in the heated $TbPc_2$ sample.

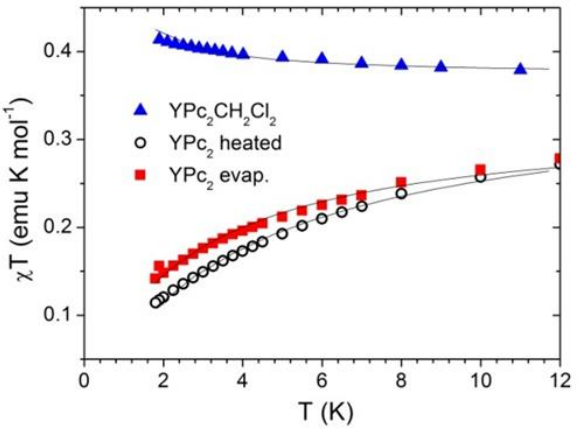

Fig 3.12: Temperature dependence of the relaxation time extracted from ac susceptibility data on the pristine (red) and heated (blue) $TbPc_2$ samples. The empty symbols correspond to measurement in a static magnetic field of 5 kOe. The black lines correspond to the best fit curves obtained using the Curie–Weiss law.

It is now evident that a more accurate characterisation of the sublimated molecular films of $TbPc_2$ is mandatory in order to understand its peculiar magnetic behaviour, i. e. the observation of a

hysteretic behaviour not observed in the heated powders used to evaporate the film. We will present later more detailed investigations based on large scale facilities such as the Swiss muon source, which can provide insight on the magnetic properties of the evaporated films. We discuss here *in house* magnetic circular dichroism, MCD, investigations. Although MCD cannot offer the same high potentiality of the formerly mentioned large scale facilities techniques, it is able to provide interesting information concerning the preferential molecular orientation respect to the substrate surface.

3.2.6 Magnetic Circular Dichroism on $TbPc_2$ sublimated on quartz

We performed angle-resolved Magnetic Circular Dichroic (MCD) spectroscopy at room temperature under 13 kOe of applied field on a film of thickness (ca. 200 nm, thus equivalent to that of previously investigated samples) evaporated on a diamagnetic quartz substrate hold at room temperature [37]. The spectra were acquired for three different values of the ϕ angle formed by the magnetic field and propagation vector of the light with the normal to the surface, namely ϕ= 0°, 22°, 45°. The data, reported in fig 3.13, are compared to those obtained for a CH_2Cl_2 solution of the complex, taken as an isotropic reference.

We focused our attention on the Q-band region of $LnPc_2$ molecules around 670 nm, related to the family of $\pi^* \rightarrow \pi$ transitions centred on the Pc^- ligands. Such transitions are known to be polarised on the Pc plane, thus giving precious information on the orientation of the molecule [38]. A strong angular dependence is observed in the evaporated sample, the shape of the MCD evolving from dispersive- to absorptive-like. If we compare the three spectra of the evaporated sample with that of the solution, we notice that the line shape evolution likely originates from the relative weight of different spectral components which can all be found in the isotropic MCD spectrum. This suggests a more complex structure of the electric dipole orientations in the Q-band of $TbPc_2$ with respect to the simple

Pc ligand. While this topic needs further dedicated studies, it is clear that molecular orientation is responsible for this angle-dependent behaviour.

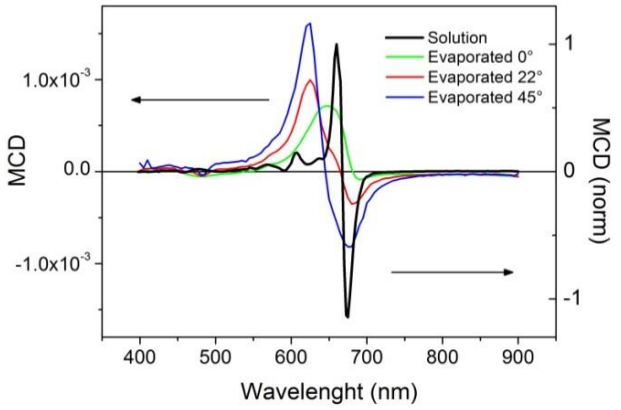

Fig 3.13: Room temperature MCD spectra (under 13 kOe applied field) of $TbPc_2$ as a CH_2Cl_2 solution (black, normalized to the positive peak) and as 200 nm evaporated film at different angles of incidence of the light with respect to the surface normal (green, red, blue, actual signal magnitude).

In order to gain further insight on the anisotropy of the evaporated film we studied the field dependence of the MCD signal measured at λ= 605 nm and T = 1.8 K. The observation of the magnetic behaviour through π optical transitions of the ligand is due to a partial hybridization of these orbitals with those of the metal [39]. As shown in fig. 3.14, the typical butterfly hysteresis is found at ϕ= 45°; for ϕ= 0°, however, the hysteresis loop closes significantly, suggesting that $TbPc_2$ molecules organize themselves in the evaporated film with their tetragonal symmetry axis lying in the plane of the substrate. A preferential orientation of $TbPc_2$ on oxide surfaces in the standing configuration, characterises simpler Pc molecules and confirms previous experiments on $TbPc_2$ based on synchrotron radiation [13].

Observation of a hysteresis seems therefore to be associated with the order in the crystal packing also not directly related to dipolar or exchange interactions.

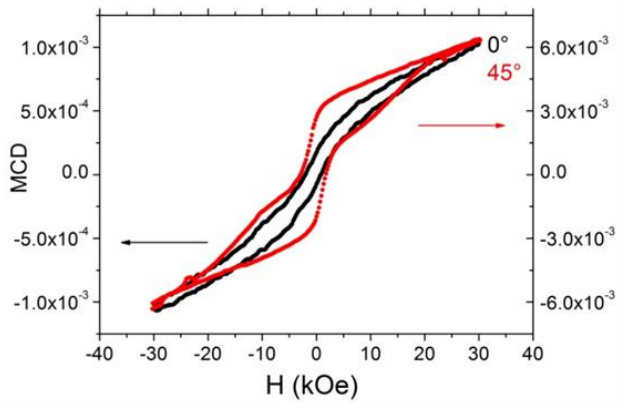

Fig 3.14: Low temperature (1.8 K) MCD hysteresis loops of a 200 nm $TbPc_2$ thin film evaporated on quartz. The loops were recorded at λ= 605 nm and with light incidence of 0° (black) and 45° (red) with respect to the surface normal. The sweeping rate is 150 Oe s^{-1}.

3.3 Characterisation of thick films through low-energy implanted muons

In the previous section a magnetic characterisation of the pristine and heated powders has been reported. In order to complete the magnetic characterisation of the sublimated films and shed some light on the different behaviour of thin and thick films Low-Energy implanted Muon Spin Relaxation (LE-μSR) experiments were carried out [13]. The investigation was performed thanks to the collaboration with Dr. Zaher Salman of the Paul Scherrer Institute (PSI) which carried out also the data analysis.

The unique properties of this technique allow a depth characterisation of the dynamics of the magnetic moments inside the films. Before starting our discussion a brief introduction to the basic concepts of the technique is presented here. Muons can be employed as local probe to detect dipolar fields. In fact, the positive muons are leptons with charge +e, spin $\frac{1}{2}$, rest mass m_μ= 207m_e and a gyromagnetic ratio $\gamma/(2\pi)$ of= 135.5 MHz/T. A 100% polarised beam of muons can be generated and focalised on the investigated sample.

The penetration depth of the muons depends on their energy, i.e. the more energy the more are penetrating (fig. 3.15).

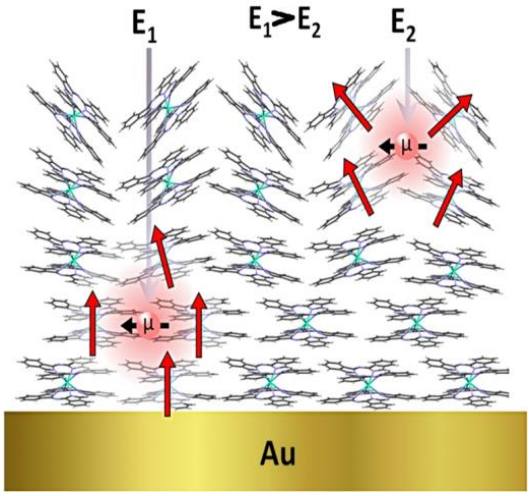

Fig 3.15: Schematic of a typical LE-μSR experiment. Fully spin-polarised muons are implanted with energy E into a thin film of $TbPc_2$ and sense the dipolar magnetic fields from moments of neighbouring SMMs. The muon mean implantation depth is proportional to their energy E.

The muons are affected by the local fields inside the sample, which induces a change in the initial polarisation because the muons magnetic moments precess around the local static field. However, they are not long living particles (mean lifetime is 2.2 μs) and after a time of the order of few μs they decay:

$$\mu^+ \rightarrow e^+ + \upsilon_e + \bar{\upsilon}_\mu \qquad (3.3)$$

this decay includes the emission of an electron neutrinos υ_e, a muon antineutrinos $\bar{\upsilon}_\mu$ and a positrons e^+.

Positrons are preferentially emitted along the muons' spin polarisation at the moment of the decay (fig. 3.16). In fact, the probability of the positrons emission in a direction forming a θ angle with the muon polarisation can be calculate as:

$$W^+(\theta, \varepsilon) = 1 + A^+(\varepsilon)\cos\theta \qquad (3.4)$$

where ε is the energy of the positron and A^+ is the asymmetry. Thus, counting the spatial distribution of the emitted positrons allows to follow the time evolution of the muons polarisation. From this data is thus possible to get information on the local field experienced by the muons.

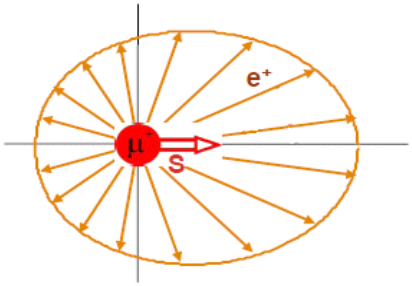

Fig. 3.16: Preferential emission of the positron along the polarisation axis of the muon.

In these experiments, fully spin-polarised muons are implanted into the sample and used as a local probe to detect dipolar fields from the surrounding molecules. They provide the direct observation of the spin dynamics of individual SMMs.

In this study three samples were investigated: (1) a microcrystalline powder sample of $TbPc_2 \cdot CH_2Cl_2$, (2) a thick (ca. 1 μm) and (3) a thinner film sample (ca. 100 nm). The films were evaporated onto 200 nm polycrystalline gold films grown on freshly cleaved Muscovite mica substrates. The thickness of the film was estimated by atomic force microscopy (AFM) with the standard scratch method and crosschecked by magnetometry measurements [40]. The sublimation rate was estimate using the following procedure. A $TbPc_2$ film was sublimated on quartz for at list one hour. The sample was then undergone to scratch and AFM investigations. The scratch procedure was carried out by using a thin needle in order to selectively remove in the scratched area (ca 40μm per several mm) the $TbPc_2$ deposit from the quartz substrate. The AFM was then used to trace the step profile and get the thickness information. Thus the thickness allows the calculation of the deposition rate. It's important to note that for film deposited on

Au(111) grown on mica this procedure cannot be employed because the substrate is not hard enough and it can be damaged by the scratch procedure. During the samples preparation it was impossible, for geometric reason, to prepare in parallel films on Au(111) and on a quartz substrate because the size of sample required for μSR is very large (3 cm of diameter disks). This made impossible a direct scratch measure of the sample thickness. However, the deposition rate during the film growth was estimated by measuring the sublimation rate before and after the sample preparation.

The thickness data were then crosschecked after the muon experiment by magnetometry measurements. To do that each $TbPc_2$ film was re-solubilised in CH_2Cl_2. The solution was dried onto a stretched Teflon tape to obtain the $TbPc_2$ solid which was investigated by standard magnetometry. The saturation magnetisation of the sample M_{sample} was then measured. Knowing the molar magnetisation M it was possible to get the total mass of the sample as:

$$Mass = \frac{M_{sample}}{M} \cdot M_w \qquad (3.5)$$

where M_w is the molecular weight. Thus knowing the surface area of each sample and the density of the $TbPc_2$ film it was possible to calculate the thickness. This estimation of the thickness was found in good agreement with the one obtained from AFM experiment (96 nm vs 107 nm for thinner film).

The muon spin relaxation curves obtained for the microcrystalline powder and the thick film sample in zero field, where in ordinate the measured asymmetry is reported, are represented in fig. 3.17. The measurements in both samples show a remarkable qualitative similarity in the whole temperature range. In high temperatures, i.e. above 100 K the curves show an exponential-like relaxation from the initial value to zero. At 4.2 K the asymmetry exhibits a dip at early times (inset of fig. 3.17), followed by a recovery and then relaxation at longer times. The slowly relaxing tail indicates that the internal magnetic field experienced by the

implanted muons in $TbPc_2$ contains two contributions: a static component and a dynamic component. The static and dynamics terms are relative to the $\upsilon/(\gamma\delta)$ ratio, where the υ is the fluctuation rate of the dynamic magnetic field, $\gamma/(2\pi)$= 135.5 MHz/T is the muon's gyromagnetic ratio, and δ is the width of static magnetic field distribution sensed by the muons. The static case is approached when the ratio is $\ll$1, while the fast fluctuation limit is approached when the ratio is $\gg$1. When muons experience a distribution of static magnetic fields with an additional dynamic component, the muon spin relaxation curve can be described by the phenomenological static Kubo–Toyabe function, multiplied by a suitable dynamic relaxation [41,42]. The form of the Kubo–Toyabe function depends on the distribution of the static field sensed by the implanted muons, e.g., Gaussian or Lorentian.

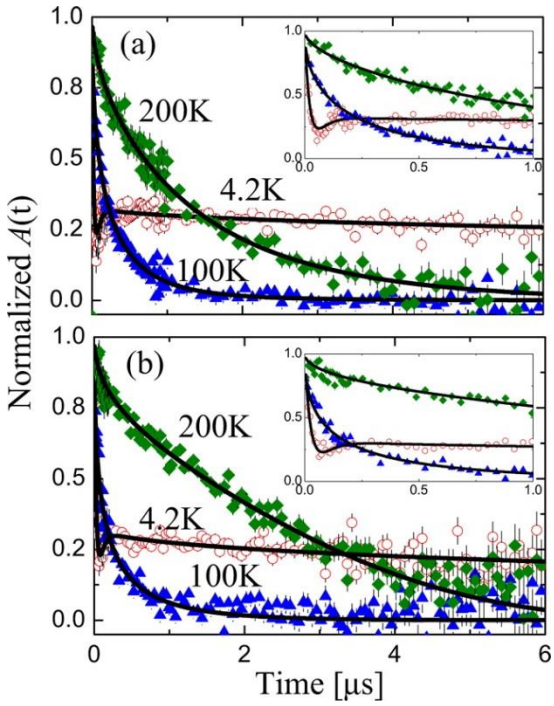

Fig. 3.17: Typical muon spin relaxation curves in the (a) bulk and (b) thick film samples measured in zero applied field and at various temperatures. The insets show the early time relaxation, where the dip in the relaxation can be clearly seen at low temperatures. The lines are fits to equation 3.6.

In our case, the asymmetry measured for all $TbPc_2$ samples at all the investigated temperatures was found to fit best to a Lorentian Kubo–Toyabe multiplied by a square root exponential relaxation:

$$A(t) = \frac{A_0}{3}\left[1 + 2(1-\gamma\delta)e^{-\gamma\delta t}\right]e^{-\sqrt{\lambda t}} \qquad (3.6)$$

where A_0 is the initial asymmetry and λ is the relaxation rate, which contains information regarding the dynamics of the local field. The square root relaxation reflects the averaging of the relaxation behaviour of muons stopping in many non-equivalent sites [26,43–47]. By fitting the data with the above mentioned equation the parameters λ and δ were obtained and their temperature dependence is shown fig. 3.18.

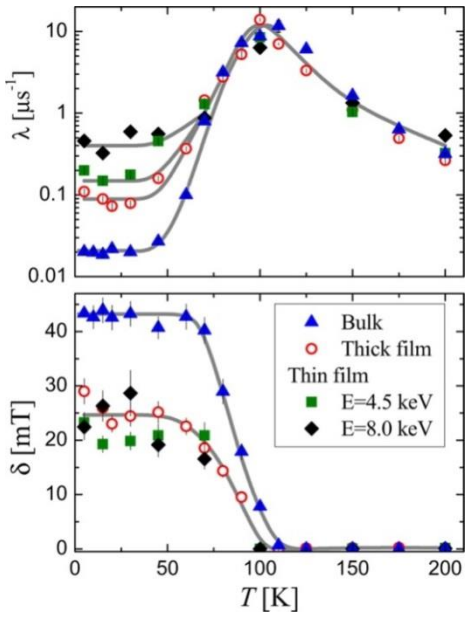

Fig. 3.18: λ (top) and δ (bottom) as a function of temperature in bulk, thick and thin film samples obtained from fits of the relaxation curves to equation 3.6. The lines are a guide to the eye.

It is important to note that the results obtained for the microcrystalline powder are consistent with previous muon spin relaxation measurements [26].The qualitative similarity between bulk

and films behaviour is an indication that SMM nature of the $TbPc_2$ in the film is retained. The static and the dynamic behaviour in all the three samples are in fact characterised by three different temperature regimes. At high temperature λ is small and δ is ca. zero. As the temperature is decreased λ increases sharply while δ remains zero. At ca. 100 K, λ peaks and δ becomes non zero. Finally, below ca. 50 K both the parameters saturate and become temperature independent. However, quantitative differences are observed at low temperature between the microcrystalline powder and the films; for example, the saturation value of δ is ca. 42 mT in the powder and ca. 24 mT in the film samples. It is important to point out that δ is equal in both film samples throughout the whole temperature range and is even independent of the muons' implantation energy. At high temperature, λ, which is directly related to the spin dynamics, is also equal in both films and is E independent. However, at low temperature, and only in the thin (nominally 100 nm) film, it strongly depends on E.

We consider first the static magnetic field experienced by the muons. At high temperatures, δ is ca. zero reflecting the absence of static fields as a consequence of fast thermal fluctuation between the ground ($J_z = \pm 6$) and the first excited ($J_z = \pm 5$) spin states. The saturation of δ at low temperature indicates that muons experience a temperature-independent distribution of static fields. In fact, at this temperature we expect all the molecules to reside in the ground state, since the energy gap to the next excited state is more than 650 K. Information regarding the dynamics of the local field can be extrapolated from λ. The exponential increase as the temperature is decreased in the high temperature regime demonstrates the slowing of spin dynamics. This is due to the reduced probability of spin-phonon-mediated transitions between different spin states [44,48,49]. The small difference in the λ value between the microcrystalline powder and the films in this temperature regime implies that the energy gap between the ground and the first excited state does not change significantly. This is a direct evidence that there is almost no change in the crystal field of the Tb^{3+} ions

between microcrystalline powder and films. In contrast to this behaviour, the saturation of λ at low temperature is a consequence of persistent spin dynamics at temperatures far below the energy gap. This is attributed to quantum tunnelling between the two quasi-degenerate $J_z = \pm 6$ ground states [26,47], which is particularly efficient in zero applied magnetic field, corresponding to the condition of our experiment. Interestingly, in fig. 3.18 one can observe a clear difference in the saturation value of λ depending on the sample: bulk, thick or 100 nm film. Moreover, in the 100 nm film it also depends on the muons' implantation energy/depth.

In what follows we extract the correlation time of the molecular spin dynamics as a function of temperature. At low temperatures where $\gamma\delta > \lambda$, $A(t)$ is almost identical to the dynamic Lorentzian Kubo-Toyabe function, and hence $\lambda = (2/3\tau)$ [43,50], where τ is the correlation time of the local magnetic field experienced by the muon, which in our case is that generated by the $TbPc_2$ SMMs. However, at high temperatures, where δ is ca. 0, the relaxation rate can be written as $\lambda = 2\tau(\gamma\delta_0)^2$ [43,50], where δ_0 is the size of the fluctuating field at the measured temperature. Note that the SMMs are in their ground J = 6 manifold throughout the measured temperature range. Therefore, δ_0 can be evaluated from the low-temperature saturation value, $\delta_0 = \delta(T \to 0)$, which reflects the size of the dipolar field from the magnetic moment of a single $TbPc_2$ molecule. Thus, we can readily extract τ as a function of temperature in the high and low-temperature ranges, as shown in fig. 3.19.

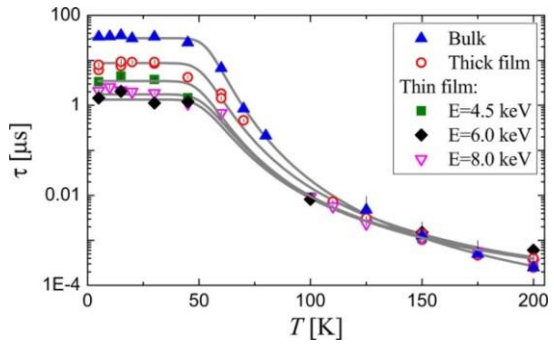

Fig. 3.19: Correlation time as a function of temperature measured in bulk and $TbPc_2$ films. The lines are fits to equation 3.8.

The probability (or inverse correlation time) of phonon-induced transitions between the $J_z = \pm 6$ and $J_z = \pm 5$ states is [44,48,49]:

$$\frac{1}{\tau_{sp}} = C\Delta^3 \exp\left(\frac{\Delta}{T}\right) \qquad (3.7)$$

where C is a temperature-independent parameter that represents the spin-phonon coupling strength and Δ is the energy gap between the spin states. This accounts for the observed high-temperature dependence of τ, but given the exponential dependence and the large value of Δ, no spin dynamics is expected at low temperatures. However, in the low-temperature regime of our muon spin relaxation data we find that τ is finite and temperature- independent. In order to model these results, we add a phenomenological constant contribution at low temperatures, τ_q, which reflects the contribution of quantum tunnelling to the correlation time. Thus, the full probability for transitions between different sublevels of the J = 6 manifold is [49]:

$$\frac{1}{\tau} = \frac{1}{\tau_{sp}} + \frac{1}{\tau_q} \qquad (3.8)$$

A fit of the results to this model provides the values for Δ, C, and τ_q given in table 3.2. We find that Δ is similar in all samples and exhibits no implantation energy dependence, as expected from the similar high-temperature behaviour in τ. This confirms that the crystal field experienced by the Tb ions does not depend on sample or depth in the films. The values of C vary significantly between the different samples. This is to be expected between bulk and films, given the loss of solvent molecules of CH_2Cl_2 [23] and the probable formation of a different molecular order in the films. These effects modify the phonon spectrum dramatically and, therefore, affect the value of C. However, the difference between the thick and 100 nm film is surprising, but may also be due to the effect of film thickness on the phonon spectrum when it is decreased from the micrometer to the nanoscale.

Parameters	Bulk	Thick film (~1μm)	Thin film (~100nm)
C [10^{-14}/μs·K^3]	6.2±2.5	1.1±0.2	0.51±0.22
Δ [K]	877±30	790±10	640±30
τ_q	31.2±1.6	6.6±0.2	See fig. 3.20

Table 3.2: Summary of parameters from fits of τ as a function of T to equation 3.8.

Most importantly, we note that only in the thin film we find a clear E/depth dependence of τ_q, as shown in fig. 3.20. To establish a clear relation between the muons' implantation energy and the mean/root mean squared (rms) stopping depth in the $TbPc_2$ film (fig. 3.20), Trim. SP simulations [51] were used to model experimental measurements. First, the fraction of the asymmetry was determined from muons stopping in the gold substrate as a function of E. For this purpose, $A(t)$ was measured in a magnetic field, B, applied transverse to the initial spin of the muons. At 5 K muons stopping in the $TbPc_2$ film depolarise very rapidly due to the large internal fields, while muons stopping in nonmagnetic gold experience predominantly the applied transverse field and, therefore, precesses at the Larmor frequency, γB.

The normalized fraction of precessing signal as a function of E is plotted in fig. 3.21. Next, the muon stopping depth profile in a $TbPc_2$ film of density ρ ca. 1.5 ± 0.1 g·cm^{-3} was simulated. We further assume that our muon beam (radius ~1cm) impinges on a film with thickness cross-section profile as illustrated in the inset of fig. 3.21, which is suggested by AFM measurements. Best fit to the experimental data is obtained using a film with a nominal thickness of ~100 nm, which falls gradually to~50 nm at the edges of the beam spot. Note that this method of implantation depth estimate has many potential systematic uncertainties due to the non-uniform thickness profile and density of the film.

However, this treatment gives a rough idea of the depth dependence of τ_q as reported in fig. 3.20. Here, the values of τ_q are basically a weighted average of the correlation time of the $TbPc_2$ molecules over the full stopping depth distribution of the implanted muons, which provides qualitative information regarding its depth

dependence. Interestingly we notice that the depth dependence extends to a scale of several tens of nm away from the gold surface.

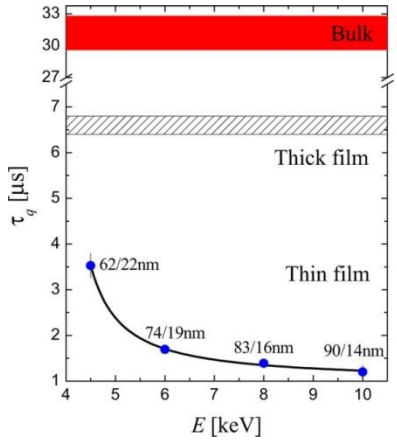

Fig. 3.20: τ_q as a function of E (and corresponding mean/rms implantation depth) obtained from fits of τ as a function of temperature to equation 3.8. The solid-shaded and hatched areas represent the values (and uncertainty) in the bulk and the thick film samples, respectively.

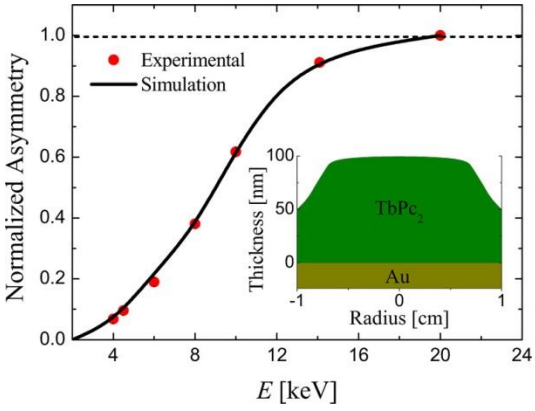

Fig. 3.21: Normalized fraction of muons stopping in the Au substrate as a function of E. The solid line is the estimated value from Trim.SP simulations using a $TbPc_2$ film with a nominal thickness of~100nmand a cross-section profile as illustrated in the inset.

As mentioned in the section 3.1 the starting point of these studies were the XMCD and XNLD measured on a $TbPc_2$ thick film and on the monolayer [13]. The different magnetic behaviour of the two samples was attributed to a competition between molecule–

substrate and molecule–molecule interactions. It's now interesting to compare the muon spin relaxation data to previous measurements. The XMCD and XNLD techniques are sensitive only to the top few monolayers and they do not provide details of the depth dependence of the $TbPc_2$ magnetic and structural properties. Muon spin relaxation measurements complement the magnetic characterisation by revealing a significant depth dependence of the molecular spin dynamics as far as several tens of nm from the surface. In particular, τ_q is small for high E, i.e., near the gold surface and becomes larger as we probe molecules further away from the substrate, gradually approaching the value measured in the thick film where all muons stop far from the substrate (few 100's nm away). The data are in agreement with the XMCD detected hysteresis loops which show no hysteresis opening in monolayer samples [13,14,21] and the recovery of the hysteresis opening in the thick film [13]. This finding, in conjunction with the different orientation of the molecules highlighted by XNLD in thick and monolayer films, suggests that molecule–molecule interactions play a key role in the magnetisation dynamics of the $TbPc_2$ films. In fact the depth dependence of τ_q may be related to a gradual variation of the molecular packing from the lie down geometry in proximity of the metal substrate to the standing up characterising the top layers of the thick film. It is important to note that this interpretation is in agreement with what shown in the previous paragraph about pristine and heated powder.

3.4 Toward $TbPc_2$ spintronic devices

3.4.1 Introduction:

$TbPc_2$, as well as all SMMs, have been a workbench for the study of quantum effects in magnetism [27]; more recently these systems have attracted a growing interest as active elements in organic spintronic devices (OSPDs) [52]. These generally consist of a

semiconductor organic film located between two ferromagnetic electrodes, one acting as spin injector and the other as spin analyser [52](fig. 3.22).

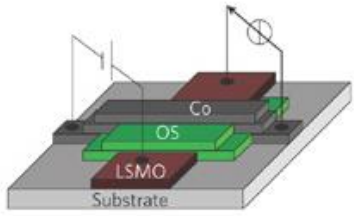

Fig. 3.22: Schematic representation of a vertical spin valve device. The organic film (OS) is stratified between the two ferromagnetic electrodes of cobalt (spin injector) and Lanthanum Strontium Manganite Oxide (LSMO)(spin analyser). Thanks to A. V. Dediu [52].

Recent studies, employing tris(8-hydroxyquinolinato) aluminium (Alq_3) organic film, have shown how OSPDs can be designed to behave as spin valves or "memristor" [53] where the non-volatile resistence of the device can be tuned and depends on the hystoric current and bias voltage applied. Recent electric transport studies involving SMMs are based on single molecules transistor [54,55] where the molecule is placed between two nonmagnetic electrodes. On the other hand Wernsdorfer et al. have recently obtained a supramolecular spin valve [3] employing $TbPc_2$ molecules deposited on a carbon nanotube. At best of our knowledge, SMMs have not yet been employed as organic film in macroscopic spin valve devices.

In OSPDs the molecules-electrode interface plays a key role to define the final device properties [56]. Therefore the knowledge of the magnetic behaviour of the interface is mandatory in order to move toward OSPDs incorporating $TbPc_2$ or other SMMs as organic film.

Two of the most employed electrode materials in OSPD are the Lanthanum Strontium Manganite Oxide (LSMO) used as spin injection and the metallic cobalt as spin analyser [52]. The study of the molecules-electrode interfaces, i.e. $TbPc_2$/LSMO and $TbPc_2$/Co has been here splitted and the two hybrid surfaces, obtained by sublimation of the $TbPc_2$ on the ferromagnetic electrode surfaces,

have been studied separately. This investigation has been carried out by employing the element selectivity and surface sensitivity of X-ray absorption spectroscopy (XAS) and related techniques, like X-ray Magnetic Circular Dichroism (XMCD) (see section 2.5), which allow to distinguish the magnetic signal of the $TbPc_2$ film from the bigger one coming from the substrate. XMCD has been already successfully employed on $TbPc_2$ and for other SMMs deposited on different surfaces [13,14,21,22,57–60].

3.4.2 $TbPc_2$/LSMO/STO hybrid surface

The characterisation of such hybrid surface has been preliminary reported by Margheriti [61]. Herein it is reported only a brief summary just for the clarity of the discussion. LSMO is a perovskite manganite of formula $La_{1-X}Sr_XMnO_3$ which, for determined X values (for example 0.3), shows an excellent magnetic polarisation at room temperature [62]. Its stability under different conditions allows the preparation of *ex situ* samples. The LSMO substrates employed in our study were made by channel spark ablation from a stoichiometric polycrystalline target in partial oxygen atmosphere ($P=4x10^{-2}$ mbar) [63].

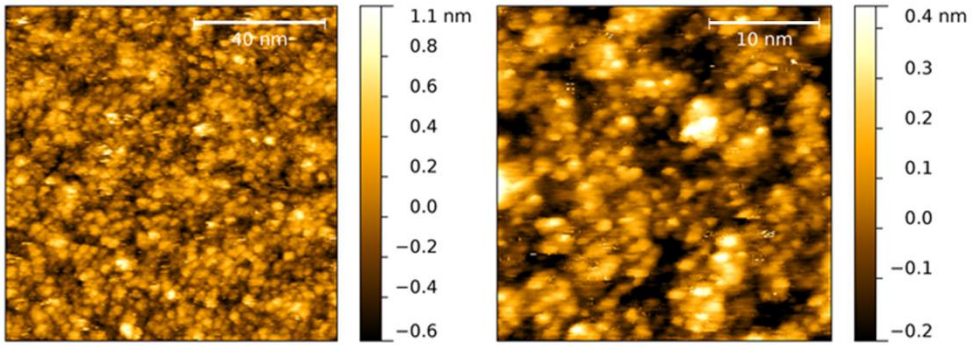

Fig. 3.23: STM images of 12 nm LSMO on STO, the surface was annealed 30 minutes at 250°C in UHV before being investigated. 100x100nm² (left) and 30x30 nm² (right) both acquired with 50mV bias and 50pA of current.

The STM investigation carried out on a LSMO after that the surface

was annealed at 250°C for 30min in UHV is reported in fig. 3.23. The images reveal a granular surface with average height of ca. 1 nm (RMS roughness 0.29 nm). Most outgrowths show lateral dimensions comparable with those of the $TbPc_2$ molecules (ca. 1.5 nm). Thus the surface corrugation does not allow the STM characterisation of sub-monolayer $TbPc_2$ films.

The X-ray absorption spectroscopy characterisation was performed at the SIM-X11MA beamline at the Swiss Light Source (SLS) synchrotron facility by *in situ* deposition of a thin molecular layer. The LSMO substrate, consisting in a 12 nm LSMO film grown on strontium titanium oxide (STO), was cleaned by sonication in isopropanol before being used. The molecular sublimation was carried out using the device described in section 2.2. A thin film of $TbPc_2$ was sublimated *in situ* in UHV condition on 12 nm thick film of LSMO substrate. The XAS investigation of the hybrid surface was performed at the Mn $L_{2,3}$ and Tb $M_{4,5}$ edges. The spectra were acquired in total electron yield mode using both linearly and circularly polarisation light. The magnetic field was applied along the photon propagation vector (fig. 3.24 left) and at variable angle, θ, with the normal to the surface (fig. 3.24 right).

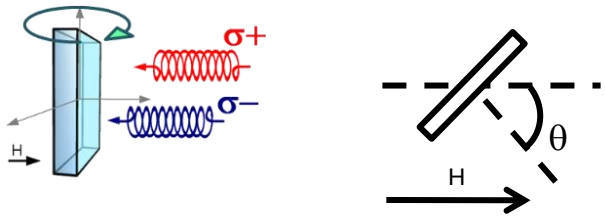

Fig. 3.24: Schematic representation of the geometry used in XMCD experiment. The field is applied along the photon direction (left); θ is the angle between the magnetic field direction and the normal to the surface (right).

In fig. 3.25 are reported the XAS spectra acquired at 2 K and in presence of a 3 T field for both circular polarisations, i.e. σ^+ and σ^- corresponding to right and left polarisation, respectively, as well as the XMCD signal defined as $\sigma^- - \sigma^+$. The curves show the characteristic features expected for LSMO films reported by other authors [64], confirming the quality of our surface, especially in respect of its magnetic polarisation.

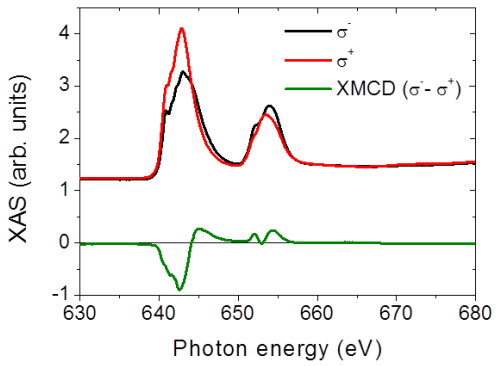

Fig. 3.25: XAS spectra acquired at the Mn $L_{2,3}$ edges in right circular polarisation σ^- (black) and left polarisation σ^+ (red) and the XMCD spectrum $\sigma^- - \sigma^+$ (green) of the $TbPc_2$/LSMO/STO hybrid surface.

The field dependence of the XMCD signal was recorded at the Mn $L_{2,3}$ at two angles, θ, between the magnetic field and the surface. Fig. 3.26 shows a more rapid saturation of the magnetic signal for θ = 45° in agreement with the expected angular dependence for the in-plane magnetic anisotropy of LSMO films.

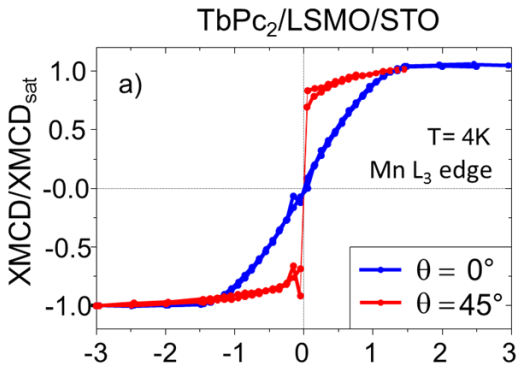

Fig. 3.26: Field and angular dependence of the XMCD signal acquired at the Mn L_3 edge.

The sample was then characterised at the Tb $M_{4,5}$ edges in order to get structural and magnetic information on the molecular film. Since the roughness of the LSMO does not allow an STM investigation to get information about the molecular orientation on the surface, linearly polarisation light was employed (see section 2.5.4).

The XAS spectra using vertically (σ^V) and horizontally (σ^H) polarised light were recorded at Θ = 45° thus allowing to extract the X-ray natural linear dichroism (XNLD) spectrum, defined as $\sigma^V - \sigma^H$, which is reported in fig. 3.27. The presence of dichroism at the M_5 edge suggests a non random orientation of the electric field generated by the ligands around the Tb^{3+} ion and thus a partial preferred orientation of the molecules on the surface can be suggested. By comparison with previous calculated data reported in literature [13] the shape of the XNLD spectrum can be interpreted considering a favoured standing-up geometry of the $TbPc_2$ molecules respect to the surface plane. This finding is in line with the observed growing mode of simple metal-phatahlocyanines on oxides [24]. Nevertheless the roughness itself could play a non-negligible role.

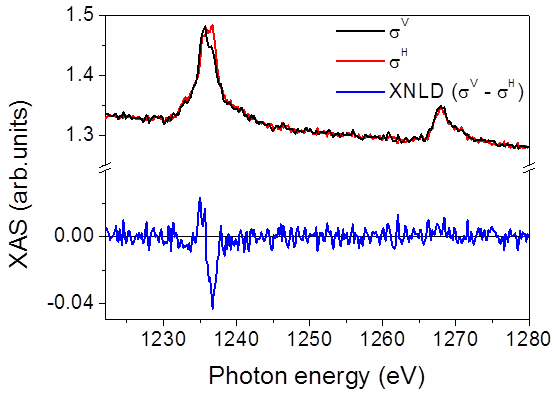

Fig. 3.27: XAS spectra acquired at the Tb $M_{4,5}$ edges in horizontal linearly polarisation σ^H (red) and vertical polarisation σ^V (black) and the XNLD spectrum σ^V - σ^H (green) of the $TbPc_2$/LSMO/STO hybrid surface.

The magnetic characterisation was carried out employing the circular polarised light. The XAS and XMCD spectra are reported in fig. 3.28. The XMCD spectrum shows a strong dichroism at the M_5 edge whereas a smaller one at the M_4 edge as expected for the $TbPc_2$ molecules [13].

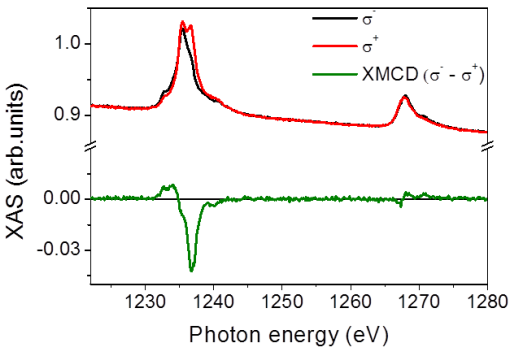

Fig. 3.28: XAS spectra acquired at the Tb $M_{4,5}$ edges in right circular polarisation σ^-(black) and left polarisation σ^+ (red) and the XMCD spectrum $\sigma^- - \sigma^+$ (green) of the $TbPc_2$/LSMO/STO hybrid surface.

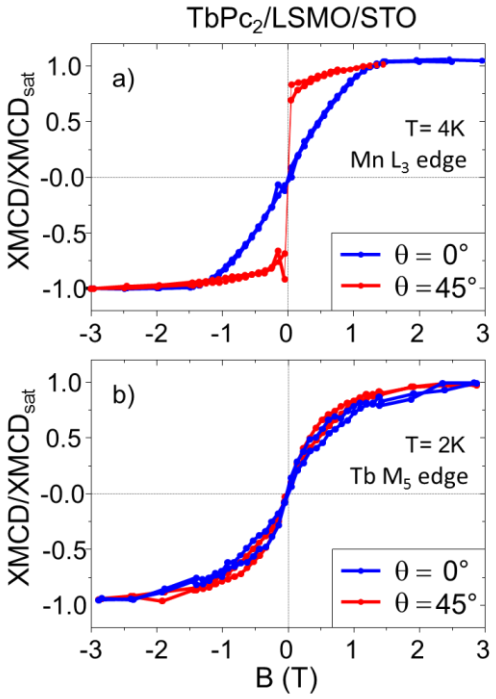

Fig. 3.29: Field and angular dependence of: the XMCD signal acquired at the Mn L_3 edge (top), and of the XMCD signal acquired at the Tb M_5 edge for the $TbPc_2$/LSMO/STO hybrid surface.

The hysteresis loops recoded at Tb $M_{4,5}$ edges are reported in fig. 3.29. Albeit the hysteresis curves show the butterfly shape, typical of bulk $TbPc_2$ molecules, the opening is significantly smaller. A slight angular dependence confirms what evidenced by the XNLD spectrum, i.e. a slightly preferential orientation of the molecules with

their easy magnetisation axis in the plane of the surface. It's interesting to note that no sizable antiferromagnetic coupling of the molecules with the LSMO was detected and no correlation of the molecular hysteresis loops with those of the substrate was observed.

The roughness of the substrate and the standing preferential orientation of $TbPc_2$ molecules are not favourable conditions to promote a significant molecule-substrate magnetic interaction and the use of magnetic metallic surface appears more promising and has been the object of this thesis, as described in the next session.

3.4.3 $TbPc_2$/Co/Cu(100) hybrid surface

The study of the hybrid surface made by phthalocyanine molecules sublimated on magnetic metals is attracting an increasing interest. Although in some cases the magnetic moment of MPc molecules is quenched by the interaction with a metallic surface [65,66], the interaction of flat metal complexes with ferromagnetic substrate has been widely studied showing interesting proprieties. By investigating the hybrid surface made by iron porphyrin molecule sublimate on Co and Ni surfaces Wende et al. [67] detected the presence of a ferromagnetic exchange coupling. Similar studies are reported also for MPc hybrid surfaces which demonstrated that the coupling can be strong enough to polarise the molecular magnetic moment at room temperature [67–69]. These findings have boosted the characterisation of hybrid surface made by $TbPc_2$ SMM on such magnetic substrates.

A recent study has shown the presence of a strong antiferromagnetic (AF) interaction between the $TbPc_2$ molecules and a nickel substrate film grown on Cu(001) [21]. Given the relevance of metallic cobalt substrate in the realization of organic spintronic devices [52] the extension of the investigation to this metallic surface appeared necessary. Only after we performed our experiments a brief report on the characterisation of the $TbPc_2$/Co/Cu(100) system became available in literature [70],

showing a weak AF coupling between $TbPc_2$ and cobalt. We will show in the following that different results have been obtained by us.

In contrast to the case of LSMO the cobalt substrate need to be prepared *in situ* at the synchrotron facility and its realization poses some criticalities. Therefore in house preliminary cobalt evaporation tests to obtain an epitaxial growth of Co on a Cu(100) single crystal were carried out in our UHV multi-instrument system presented in section 2.9.

3.4.3.1 In house experiment

In order to evaluate the optimal conditions for the cobalt epitaxial growth several techniques were employed. The thickness of the films was estimated by cross-checking STM and XPS data. The XPS regions of Co *2p* and Cu *2p* peaks and their relative fits of a 42 min evaporated Co film are reported in fig. 3.30a,b.

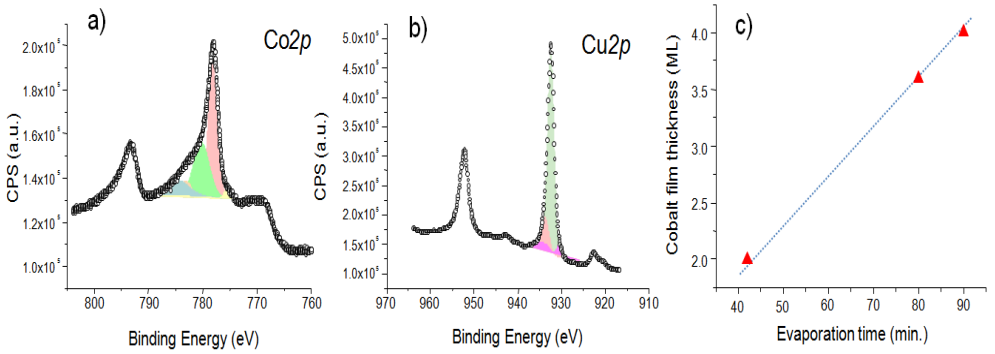

Fig. 3.30: XPS spectra and relative fit of the Co2p region (a) Cu2p region (b) and the calibration point of the evaporation process (c).

The spectra were acquired using the monochromatic Al K_α source, 1486.6 eV. Following the considerations reported in section 2.4.1 the cobalt layer thickness d was calculated as:

$$d = \lambda cos\theta \ln\left(\frac{I'_A \sigma_B}{I'_B \sigma_A} + 1\right) \qquad (3.9)$$

where λ is the escape length of the photoelectrons, I'_A , I'_B are the areas and σ_A, σ_B are the cross-section of the Cu $2p_{3/2}$ and Co $2p_{3/2}$ peaks, respectively. The calculated thickness of the 42 min evaporated cobalt film was 2.1 ML. Same investigations were repeated increasing the evaporation time obtaining the calibration curves reported in fig. 3.30c. The data could be fitted by a linear relation, as expected for constant Co evaporation flux.

Before the XPS investigation the 2.1 ML cobalt film sample was also characterised by STM. In fig. 3.31 are reported the STM images for two different nominal thicknesses, 2.1 and 4 ML of Co, as estimated from the previous calibration. Both samples show a *quasi* layer-by-layer growth [71] with the formation of small cobalt islands.

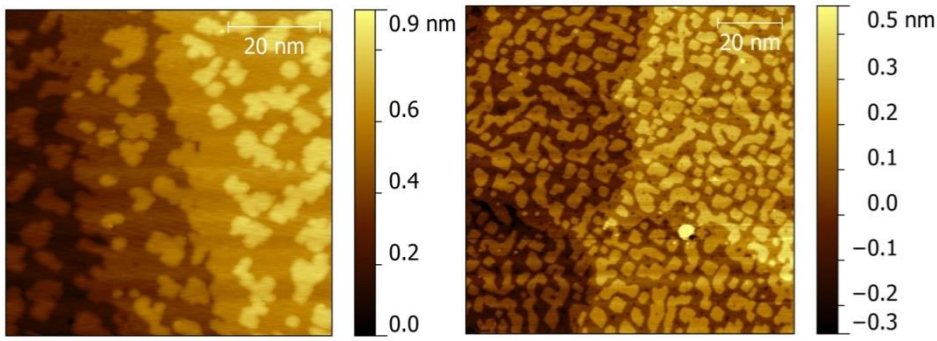

Fig. 3.31: STM image of 2.1ML (400pA; -0.4V ; 75x75nm^2) (a) and 4ML of Co on Cu(100) (900pA; 1.4V; 100x100nm^2) (b). They show the typical cobalt rounded edge islands preferentially oriented along the Cu [±110] directions.

They present rounded edges preferentially oriented along the Cu [±110] directions; moreover the cobalt films do not exactly reproduce the underling Cu atomic step edges looking meandering [72]. All these features confirm the good quality of the cobalt films.

It is well known that in thin films an intermixing of the two metals can take place even at room temperature due to an atomic exchange process [26,28]. This phenomenon could be responsible of the formation of a layer of copper on top of the cobalt film.

In order to take in account this phenomenon the LEIS

techniques, sensitive to the top-most layer chemical composition, was employed (see section 2.7). The LEIS spectra, presented in fig. 3.32, were acquired using a He^+ beam accelerated to 1000 eV on samples with increasing thickness of the Co film. The data are relative to the same samples of the XPS characterisation. The Cu peak is found at about 790 eV whereas the Co at ca. 770 eV, in agreement with atomic mass selectivity of the technique (see equation 2.26). As expected increasing the thickness deposition the intensity of the Cu peak decreases while the Co peak increases. The 4 ML sample shows almost uniquely the Co peak suggesting that for thicker samples the top-most layer is mainly made by Co.

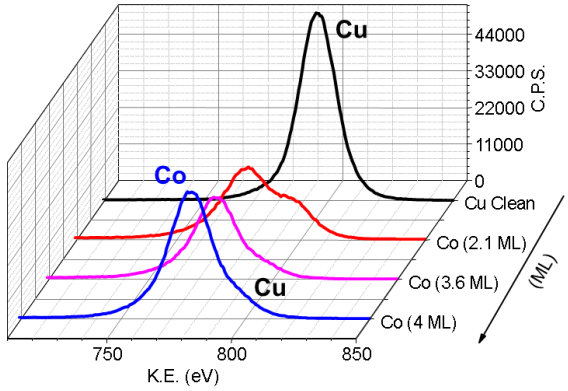

Fig. 3.32: LEIS spectra of clean Cu (100) surface (black curve) and after subsequent Co deposition: red curve, pink curve and blue curve are for 2.1 ML, 3.6 ML and 4 ML, cobalt coverage respectively.

The *in house* study was completed by STM investigation of the final hybrid surface. In order to have a clear image of the molecules sublimated on the cobalt surface a sub-monolayer coverage $TbPc_2$ film is mandatory. For this purpose we calibrated the $TbPc_2$ sublimation by STM investigation of molecular films sublimated on the Cu(100) single crystal. The image acquired on a sub-monolayer $TbPc_2$ film sublimated on Co/Cu(100) i.e. $TbPc_2$/Co/Cu(100) hybrid surface, is reported in fig. 3.33. It is important to point out that the molecules show the characteristic four lobed shape expected for lying down intact $TbPc_2$ complexes.

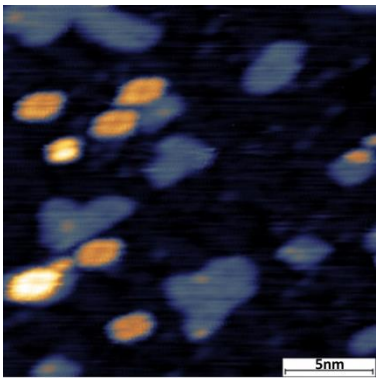

Fig. 3.33: STM image of $TbPc_2$/Co/Cu(100) (200pA; 1.5V; 22x22nm^2).

3.4.3.2 XAS characterisation

The XMCD-based investigation requires specific UHV facilities allowing the *in-situ* preparation of the hybrid surface. The samples were growth in the preparation chamber of the DEIMOS beamline at the SOLEIL synchrotron (see chapter 2.6). The cobalt evaporations were carried out using the same parameters of the *in house* experiments. Before preparing the final hybrid surface a characterisation of evaporated cobalt films was performed by using STM and XAS techniques. The nominal thicknesses presented hereafter were estimated from the Co $L_{2,3}$ edges jump ratio.

The quality of the surfaces was checked by *in situ* STM analysis. The image acquired for a nominal 2.5 ML cobalt film is reported in fig. 3.34. The image shows the expected features described in the previous chapter. Indeed the cobalt islands are aligned along two preferential directions and the edge steps look meandering (similar to what reported in fig. 3.31), as expected for the cobalt epitaxial growth on copper [71,72].

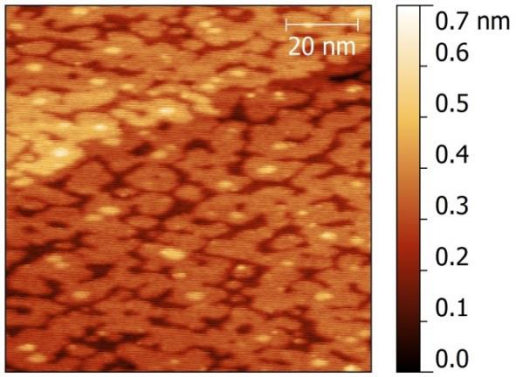

Fig. 3.34: *In situ* STM image of a 2.5 ML of Cobalt evaporated on Cu(100) (100pA ; 1.0V; 95x95nm²).

It is well known that the magnetic anisotropy of Co films depends strongly on the thickness. We decided to investigate a thickness of 5 ML which corresponds to a strong in plane magnetisation. The XAS spectra and the relative XMCD of a 5.5 ML cobalt film are reported in fig. 3.35.

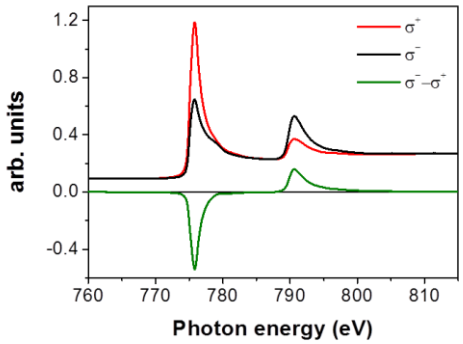

Fig. 3.35: XAS spectra acquired at the Co $L_{2,3}$ edges in right circular polarisation σ^-(black) and left polarisation σ^+ (red) and the XMCD spectrum $\sigma^- - \sigma^+$ (green) of the Co/Cu(100) surface.

It is important to note that the shape and energy of the cobalt $L_{2,3}$ rule out the presence of oxidised cobalt [73,74]. This is of the utmost importance in order to study the magnetic behaviour of the hybrid surface. In order to evaluate the magnetic behaviour of the cobalt film the XMCD sum rules can be applied [73,74]. Through their application it is possible to estimate both orbital ($\mathbf{m}_{orb}$) and spin ($\mathbf{m}_{spin}$)

moments using the integral calculation described by Chen et al. [73] (see section 2.5.3.1). From this analysis we estimated $\mathbf{m}_{orb}$ = 0.23 μ_B, $\mathbf{m}_{spin}$ = 1.81 μ_B and the resulting ratio m_{orb}/m_{spin}= 0.127. These data are in agreement with what reported in literature [74] and will be useful for further considerations.

In order to prepare the hybrid surface the sublimation of thin $TbPc_2$ film was carried out on a freshly prepared 5 ML cobalt film. We employed the elemental selectivity of the XAS based techniques to characterise the cobalt film magnetic behaviour of the $TbPc_2$/Co/Cu(100) hybrid surface. The XAS spectra acquired at the Co $L_{2,3}$ edges using both circular polarisations and the relative XMCD spectrum are reported in fig. 3.36.

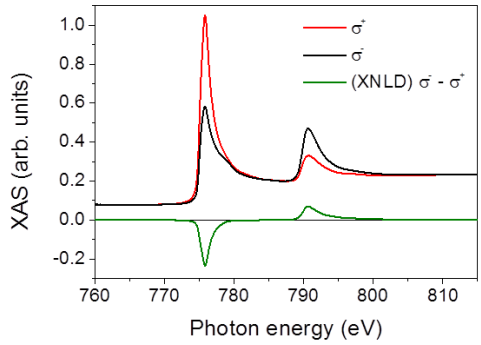

Fig. 3.36: XAS spectra acquired at the Co $L_{2,3}$ edges in right circular polarisation σ^- (black) and left polarisation σ^+ (red) and the XMCD spectrum $\sigma^- - \sigma^+$ (green) of the $TbPc_2$/Co/Cu(111) hybrid surface.

The sum rules were applied allowing the calculation of the $\mathbf{m}_{orb}$ = 0.22 μ_B, $\mathbf{m}_{spin}$ = 1.75 μ_B and the resulting ratio m_{orb}/m_{spin}= 0.125. These data are in agreement with those presented for the bare 5.5 ML cobalt film. Thus no significant modification of the magnetic behaviour of the cobalt film is showed due to the presence of the molecular film.

The field dependence of the maximum of the XMCD signal at the Co L_3 edge acquired for Θ=0° and Θ=60° are reported in fig. 3.37. The curves show the pronounced angular dependence expected for a cobalt thin film with in plane magnetic anisotropy. The out of plane magnetic signal saturates at ~3.7 T This anisotropy field is in agreement to the expected one for 5 ML cobalt film thickness [75]

confirming the high quality and good control we have achieved in the preparation of the Co substrate.

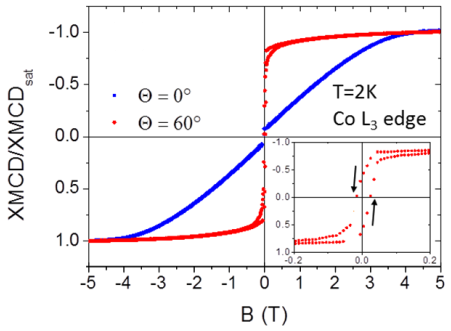

Fig. 3.37: Field and angular dependence of the XMCD signal acquired at the Co L_3 edge. In the inset is reported the enlargement of the θ=60° curve which show the hysteretic behaviour of the cobalt film.

Moving to the Tb $M_{4,5}$ edges, the XAS recorded spectra (fig. 3.38) acquired with linear polarised light show the presence of a sub-monolayer $TbPc_2$ film. A semi-quantitative estimation of the thickness can be done by comparing the Tb M_5 edge signal with the oscillation of the background that is due to the EXAFS signal of the copper substrate. Comparing our results with literature data [21,70] it is possible to assert that the $TbPc_2$ coverage is in the sub-monolayer range.

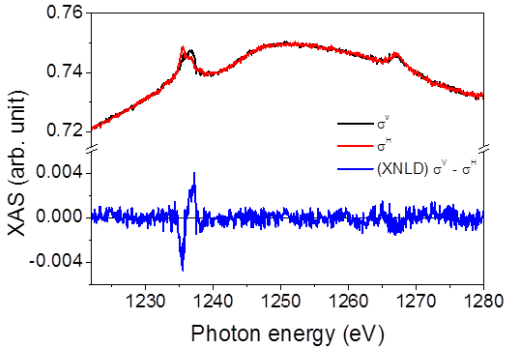

Fig. 3.38: XAS spectra acquired at the Tb $M_{4,5}$ edges in horizontal linearly polarisation σ^H (red) and vertical polarisation σ^V (black) and the XNLD spectrum σ^V - σ^H (green) of the $TbPc_2$/Co/Cu(111) hybrid surface.

The XNLD reveals a dichroic signal at the M_5 edge, whose shape is

similar to that previously observed for the film grown on LSMO, but with opposite sign. This can be ascribed to the lying down orientation of $TbPc_2$ molecules, expected for metallic surfaces and indeed observed in our STM investigation (fig. 3.33).

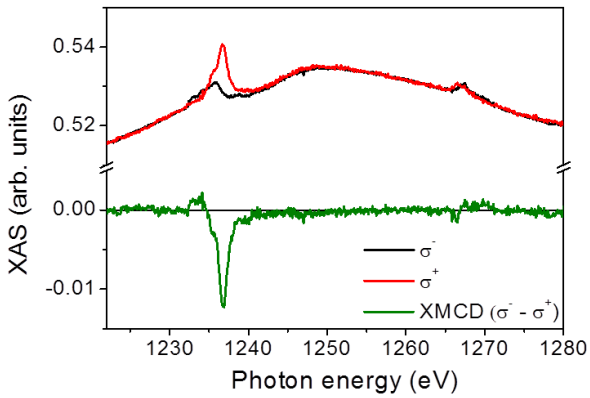

Fig. 3.39: XAS spectra acquired at the Tb $M_{4,5}$ edges in right circular polarisation σ^- (black) and left polarisation σ^+ (red) and the XMCD spectrum $\sigma^- - \sigma^+$ (green) of the $TbPc_2$/Co/Cu(111) hybrid surface.

The XMCD spectrum, reported in fig. 3.39, shows similar features to those observed also for bulk samples and films on other substrates, including the LSMO (see section 3.4.2). The field and angular dependence of the dichroic signal at the M_5 edge are reported in fig. 3.40. In agreement with previous observation, the magnetic signal saturates at smaller fields when the field is applied out of plane, θ=0°, as this corresponds to the easy axis of lying down molecules. In both loops, recorded at different angles, no detectable opening of the hysteresis is revealed. The $TbPc_2$ seems to behave as a simple paramagnetic molecule at a temperature as low as 2K, in agreement with previous findings on thin films of $TbPc_2$ evaporated on nonmagnetic substrates, such as gold [13] and copper [14].

More interesting is the absence of any detectable antiferromagnetic interaction between the molecular sub-monolayer film and the cobalt substrate. In fact the magnetic signal does not show any anomaly in the field dependence, typical of the overcoming of an antiferromagnetic interaction. It must also be noted that no correlation is observed between the magnetism of the two materials,

which present different magnetic anisotropy, and no anomalies in $TbPc_2$ behaviour are observed at the saturation fields of the Co substrate. Our results are in contrast to what recently reported by other authors [70] in a short communication for the same hybrid surface. The origin of this discrepancy remains unclear, given also the limited information available in the reported communication. In detailed analysis we performed on both Co substrate and molecular film we can exclude the incidence of the most common issues that may have a negative impact on the measure: like the formation of an oxide layer, the termination with nonmagnetic Cu film, or the evaporation of a thick molecular film, preventing a direct contact between the magnetic molecules and the magnetic substrate.

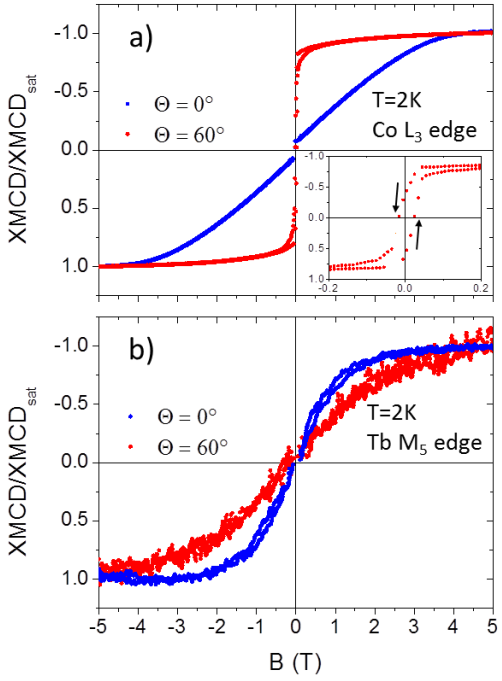

Fig. 3.40: Field and angular dependence of: the XMCD signal acquired at the Co L_3 edge (top), and of the XMCD signal acquired at the Tb M_5 edge for the $TbPc_2$/LSMO/STO hybrid surface.

References

[1] N. Ishikawa, M. Sugita, T. Ishikawa, S. Koshihara, and Y. Kaizu, J. Am. Chem. Soc. **125**, 8694 (2003).

[2] L. Bogani and W. Wernsdorfer, Nat. Mater. **7**, 179 (2008).

[3] M. Urdampilleta, S. Klyatskaya, J.-P. Cleuziou, M. Ruben, and W. Wernsdorfer, Nat. Mater. **10**, 502 (2011).

[4] K. Katoh, H. Isshiki, T. Komeda, and M. Yamashita, Chem. Asian J. **7**, 1154 (2012).

[5] K. Katoh, Y. Yoshida, M. Yamashita, H. Miyasaka, B. K. Breedlove, T. Kajiwara, S. Takaishi, N. Ishikawa, H. Isshiki, Y. F. Zhang, T. Komeda, M. Yamagishi, and J. Takeya, J. Am. Chem. Soc. **131**, 9967 (2009).

[6] A. De Cian, M. Moussavi, J. Fischer, and R. Weiss, Inorg. Chem. **24**, 3162 (1985).

[7] S. Takamatsu, T. Ishikawa, S. Koshihara, and N. Ishikawa, Inorg. Chem. **46**, 7250 (2007).

[8] M. Gonidec, E. Davies, J. McMaster, D. B. Amabilino, and J. Veciana, J. Am. Chem. Soc. **132**, 1756 (2010).

[9] P. Zhu, F. Lu, N. Pan, D. P. Arnold, S. Zhang, and J. Jiang, Eur. J. Inorg. Chem. **2004**, 510 (2004).

[10] N. Ishikawa, M. Sugita, N. Tanaka, T. Ishikawa, S. Koshihara, and Y. Kaizu, Inorg. Chem. **43**, 5498 (2004).

[11] S. Takamatsu and N. Ishikawa, Polyhedron. **26**, 1859 (2007).

[12] Y. Zhang, H. Isshiki, K. Katoh, Y. Yoshida, M. Yamashita, H. Miyasaka, B. K. Breedlove, T. Kajiwara, S. Takaishi, and T. Komeda, **113**, 14407 (2009).

[13] L. Margheriti, D. Chiappe, M. Mannini, P.-E. Car, P. Sainctavit, M.-A. Arrio, F. B. de Mongeot, J. C. Cezar, F. M. Piras, A. Magnani, E. Otero, A. Caneschi, and R. Sessoli, Adv. Mater. **22**, 5488 (2010).

[14] S. Stepanow, J. Honolka, P. Gambardella, L. Vitali, N. Abdurakhmanova, T.-C. Tseng, S. Rauschenbach, S. L. Tait, V.

Sessi, S. Klyatskaya, M. Ruben, and K. Kern, J. Am. Chem. Soc. **132**, 11900 (2010).

[15] M. Toader, M. Knupfer, D. R. T. Zahn, and M. Hietschold, J. Am. Chem. Soc. **133**, 5538 (2011).

[16] Y.-S. Fu, J. Schwöbel, S.-W. Hla, A. Dilullo, G. Hoffmann, S. Klyatskaya, M. Ruben, and R. Wiesendanger, Nano Lett. **12**, 3931 (2012).

[17] J. Schwöbel, Y. Fu, J. Brede, A. Dilullo, G. Hoffmann, S. Klyatskaya, M. Ruben, and R. Wiesendanger, Nat. Commun. **3**, 953 (2012).

[18] T. Komeda, H. Isshiki, J. Liu, Y.-F. Zhang, N. Lorente, K. Katoh, B. K. Breedlove, and M. Yamashita, Nat. Commun. **2**, 217 (2011).

[19] T. Funk, A. Deb, S. J. George, H. Wang, and S. P. Cramer, Coord. Chem. Rev. **249**, 3 (2005).

[20] A. Cornia, M. Mannini, P. Sainctavit, and R. Sessoli, Chem. Soc. Rev. **40**, 3076 (2011).

[21] A. Lodi Rizzini, C. Krull, T. Balashov, J. J. Kavich, A. Mugarza, P. S. Miedema, P. K. Thakur, V. Sessi, S. Klyatskaya, M. Ruben, S. Stepanow, and P. Gambardella, Phys. Rev. Lett. **107**, 177205 (2011).

[22] A. Lodi Rizzini, C. Krull, T. Balashov, A. Mugarza, C. Nistor, F. Yakhou, V. Sessi, S. Klyatskaya, M. Ruben, S. Stepanow, and P. Gambardella, Nano Lett. **12**, 5703 (2012).

[23] J. Paillaud, M. Drillon, A. De Cian, J. Fischer, R. Weiss, and G. Villeneuve, Phys. Rev. Lett. **67**, 244 (1991).

[24] I. Biswas, H. Peisert, M. B. Casu, B.-E. Schuster, P. Nagel, M. Merz, S. Schuppler, and T. Chassé, Phys. Status Solidi **206**, 2524 (2009).

[25] I. Biswas, H. Peisert, M. Nagel, M. B. Casu, S. Schuppler, P. Nagel, E. Pellegrin, and T. Chassé, J. Chem. Phys. **126**, 174704 (2007).

[26] F. Branzoli, P. Carretta, M. Filibian, M. J. Graf, S. Klyatskaya, M. Ruben, F. Coneri, and P. Dhakal, Phys. Rev. B **82**, 134401 (2010).

[27] D. Gatteschi, R. Sessoli, and V. Jacques, *Molecular Nanomagnets*, Oxford Univ. Press (2006).
[28] H. B. G. Casimir and F. K. du Pré, Physica **5**, 507 (1938).
[29] K. Katoh, Y. Horii, N. Yasuda, W. Wernsdorfer, K. Toriumi, B. K. Breedlove, and M. Yamashita, Dalton Trans. **41**, 13582 (2012).
[30] N. Lopez, A. V Prosvirin, H. Zhao, W. Wernsdorfer, and K. R. Dunbar, Chem. Eur. J. **15**, 11390 (2009).
[31] J. D. Rinehart and J. R. Long, Dalton Trans. **41**, 13572 (2012).
[32] F. Luis, M. J. Martínez-Pérez, O. Montero, E. Coronado, S. Cardona-Serra, C. Martí-Gastaldo, J. M. Clemente-Juan, J. Sesé, D. Drung, and T. Schurig, Phys. Rev. B **82**, 060403 (2010).
[33] P.-E. Car, M. Perfetti, M. Mannini, A. Favre, A. Caneschi, and R. Sessoli, Chem. Commun. **47**, 3751 (2011).
[34] A. Abragam and B. Bleaney, Dover, *Electron Paramagnetic Resonance of Transition Ions*, NewYork (1986).
[35] N. Ishikawa, M. Sugita, and W. Wernsdorfer, Angew. Chemie **44**, 2931 (2005).
[36] F. Branzoli, P. Carretta, M. Filibian, S. Klyatskaya, and M. Ruben, Phys. Rev. B **83**, 174419 (2011).
[37] G. Campo, *Magneto-optical investigation on nanostructured magneto-plasmonic materials*, PhD Thesis (2012).
[38] B. Bräuer, M. Fronk, D. Lehmann, D. R. T. Zahn, and G. Salvan, J. Phys. Chem. B **113**, 14957 (2009).
[39] C. L. Dunford, B. E. Williamson, and E. Krausz, J. Phys. Chem. A **104**, 3537 (2000).
[40] L. Margheriti, M. Mannini, L. Sorace, L. Gorini, D. Gatteschi, A. Caneschi, D. Chiappe, R. Moroni, F. B. de Mongeot, A. Cornia, F. M. Piras, A. Magnani, and R. Sessoli, Small **5**, 1460 (2009).
[41] Y. Fudamoto, I. Gat, M. Larkin, J. Merrin, B. Nachumi, A. Savici, Y. Uemura, G. Luke, K. Kojima, M. Hase, T. Masuda, and K. Uchinokura, Phys. Rev. B **65**, 174428 (2002).
[42] Z. Salman, S. R. Giblin, Y. Lan, a. K. Powell, R. Scheuermann, R. Tingle, and R. Sessoli, Phys. Rev. B **82**, 174427 (2010).

[43] Y. Uemura, T. Yamazaki, D. Harshman, M. Senba, and E. Ansaldo, Phys. Rev. B **31**, 546 (1985).
[44] A. Lascialfari, Z. Jang, F. Borsa, P. Carretta, and D. Gatteschi, Phys. Rev. Lett. **81**, 3773 (1998).
[45] Z. Salman, A. Keren, P. Mendels, V. Marvaud, A. Scuiller, M. Verdaguer, J. Lord, and C. Baines, Phys. Rev. B **65**, 132403 (2002).
[46] S. J. Blundell, F. L. Pratt, T. Lancaster, I. M. Marshall, C. a. Steer, S. L. Heath, J.-F. Létard, T. Sugano, D. Mihailovic, and A. Omerzu, Polyhedron. **22**, 1973 (2003).
[47] F. Branzoli, M. Filibian, P. Carretta, S. Klyatskaya, and M. Ruben, Phys. Rev. B **79**, 220404 (2009).
[48] J. Villain, F. Hartman-Boutron, R. Sessoli, and A. Rettori, Europhys. Lett. **27**, 159 (1994).
[49] Z. Salman, Cond-Mat/0209497 12 (2002).
[50] R. Hayano, Y. Uemura, J. Imazato, N. Nishida, T. Yamazaki, and R. Kubo, Phys. Rev. B **20**, 850 (1979).
[51] W. Eckstein, *Computer Simulation of Ion Solid Interaction*, Springer(1991).
[52] V. A. Dediu, L. E. Hueso, I. Bergenti, and C. Taliani, Nat. Mater. **8**, 707 (2009).
[53] M. Prezioso, A. Riminucci, P. Graziosi, I. Bergenti, R. Rakshit, R. Cecchini, A. Vianelli, F. Borgatti, N. Haag, M. Willis, A. J. Drew, W. P. Gillin, and V. a Dediu, Adv. Mater. **25**, 534 (2013).
[54] H. Heersche, Z. de Groot, J. Folk, H. van der Zant, C. Romeike, M. Wegewijs, L. Zobbi, D. Barreca, E. Tondello, and A. Cornia, Phys. Rev. Lett. **96**, 206801 (2006).
[55] M.-H. Jo, J. E. Grose, K. Baheti, M. M. Deshmukh, J. J. Sokol, E. M. Rumberger, D. N. Hendrickson, J. R. Long, H. Park, and D. C. Ralph, Nano Lett. **6**, 2014 (2006).
[56] S. Sanvito, Chem. Soc. Rev. **40**, 3336 (2011).
[57] M. Mannini, P. Sainctavit, R. Sessoli, C. Cartier dit Moulin, F. Pineider, M.-A. Arrio, A. Cornia, and D. Gatteschi, Chem. Eur. J. **14**, 7530 (2008).

[58] S. Voss, M. Burgert, M. Fonin, U. Groth, and U. Rüdiger, Dalton Trans. **7**, 499 (2008).

[59] M. Mannini, F. Pineider, P. Sainctavit, C. Danieli, E. Otero, C. Sciancalepore, A. M. Talarico, M.-A. Arrio, A. Cornia, D. Gatteschi, and R. Sessoli, Nat. Mater. **8**, 194 (2009).

[60] M. Mannini, F. Pineider, C. Danieli, F. Totti, L. Sorace, P. Sainctavit, M. Arrio, E. Otero, L. Joly, J. C. Cezar, a Cornia, and R. Sessoli, Nature **468**, 417 (2010).

[61] L. Margheriti, *Preparation and characterisation of SMM thin films obtained by UHV evaporation*, PhD Thesis (2010).

[62] V. Dediu, M. Murgia, F. C. Matacotta, C. Taliani, and S. Barbanera, Solid State Commun. **122**, 181 (2002).

[63] P. Graziosi, M. Prezioso, A. Gambardella, C. Kitts, R. K. Rakshit, A. Riminucci, I. Bergenti, F. Borgatti, C. Pernechele, M. Solzi, D. Pullini, D. Busquets-Mataix, and V. A. Dediu, Thin Solid Films **534**, 83 (2013).

[64] F. Li, Y. Zhan, T. Lee, X. Liu, A. Chikamatsu, T. Guo, H. Lin, J. C. A. Huang, and M. Fahlman, J. Phys. Chem. C **115**, 16947 (2011).

[65] A. Mugarza, R. Robles, C. Krull, R. Korytár, N. Lorente, and P. Gambardella, Phys. Rev. B **85**, 155437 (2012).

[66] S. Stepanow, P. S. Miedema, A. Mugarza, G. Ceballos, P. Moras, J. C. Cezar, C. Carbone, F. M. F. de Groot, and P. Gambardella, Phys. Rev. B **83**, 220401 (2011).

[67] H. Wende, M. Bernien, J. Luo, C. Sorg, N. Ponpandian, J. Kurde, J. Miguel, M. Piantek, X. Xu, P. Eckhold, W. Kuch, K. Baberschke, P. M. Panchmatia, B. Sanyal, P. M. Oppeneer, and O. Eriksson, Nat. Mater. **6**, 516 (2007).

[68] A. Scheybal, T. Ramsvik, R. Bertschinger, M. Putero, F. Nolting, and T. A. Jung, Chem. Phys. Lett. **411**, 214 (2005).

[69] J. Miguel, C. F. Hermanns, M. Bernien, A. Krüger, and W. Kuch, J. Phys. Chem. Lett. **2**, 1455 (2011).

[70] D. Klar, S. Klyatskaya, A. Candini, B. Krumme, K. Kummer, P. Ohresser, V. Corradini, V. de Renzi, R. Biagi, L. Joly, J.-P.

Kappler, U. Del Pennino, M. Affronte, H. Wende, and M. Ruben, Beilstein J. Nanotechnol. **4**, 320 (2013).

[71] T. Allmers and M. Donath, Surf. Sci. **605**, 1875 (2011).

[72] U. Ramsperger, A. Vaterlaus, P. Pfäffli, U. Maier, and D. Pescia, Phys. Rev. B **53**, 8001 (1996).

[73] C. Chen, Y. Idzerda, H.-J. Lin, N. Smith, G. Meigs, E. Chaban, G. Ho, E. Pellegrin, and F. Sette, Phys. Rev. Lett. **75**, 152 (1995).

[74] P. Srivastava, F. Wilhelm, a. Ney, M. Farle, H. Wende, N. Haack, G. Ceballos, and K. Baberschke, Phys. Rev. B **58**, 5701 (1998).

[75] M. Kowalewski, C. M. Schneider, and B. Heinrich, Phys. Rev. B **47**, 8748 (1993).